

1           **Process-based evaluation of ENSO simulation sensitivity to**  
2           **horizontal resolution in the Chinese Academy of Sciences FGOALS-**  
3           **f3 Climate System Model**

4  
5           Meng-Er Song<sup>1</sup>, Lin Chen<sup>1</sup>, Yongqiang Yu<sup>2</sup>, Bo An<sup>2</sup>, Jiuwei Zhao<sup>1</sup>, Hai Zhi<sup>1</sup>

6  
7           <sup>1</sup> State Key Laboratory of Climate System Prediction and Risk Management/Key Laboratory of  
8           Meteorological Disaster, Ministry of Education/Collaborative Innovation Center on Forecast and  
9           Evaluation of Meteorological Disasters, Nanjing University of Information Science and Technology,  
10          Nanjing 210044

11          <sup>2</sup> State Key Laboratory of Earth System Numerical Modeling and Application, Institute of Atmospheric  
12          Physics, Chinese Academy of Sciences, Beijing, China

13  
14  
15  
16          *Correspondence to:* Lin Chen (chenlin@nuist.edu.cn)

19 **Abstract.** El Niño-Southern Oscillation (ENSO) is the most prominent mode of interannual climate  
20 variability, its simulation performance thus represents a critical benchmark for evaluating the fidelity of  
21 coupled climate models. Increasing model resolution is an effective approach to improve the climate  
22 model performance; however, the impact of refining horizontal resolution from the hundred-kilometer  
23 scale to the tens-of-kilometer scale on ENSO simulation, as well as the underlying mechanisms, remains  
24 unclear. This study provides a process-based evaluation of ENSO behavior in two versions of the Chinese  
25 Academy of Sciences Flexible Global Ocean–Atmosphere–Land System Finite-Volume version 3  
26 (FGOALS-f3) climate system model: a low-resolution configuration (~100 km; FGOALS-f3-L, hereafter  
27 f3-L) and a high-resolution configuration (~25 km; FGOALS-f3-H, hereafter f3-H). Using a reproducible  
28 diagnostic framework, we assess how horizontal resolution influences ENSO amplitude, oscillation  
29 irregularity, key air–sea coupling processes, and high-frequency (HF) atmospheric variability. The low-  
30 resolution version severely overestimates ENSO amplitude, whereas f3-H produces amplitude closer to  
31 the observation. Process-based diagnostics show that this improvement arises from the more realistic  
32 representation of thermocline and zonal advection feedback processes in f3-H, which arises from the  
33 more realistic representation of the meridional structure of ENSO-related zonal wind stress anomalies  
34 over equatorial Pacific in f3-H and can be traced back to its improved horizontal resolution. The ENSO  
35 cycle in f3-L exhibits excessive regularity, featuring periodic warm-cold transitions; while f3-H  
36 reproduces an irregular oscillation resembling the observation. The excessive regularity in f3-L is  
37 attributed to its coarser resolution, which limits the simulation performance of tropical cyclones and  
38 consequently weakens high-frequency westerly wind activity over the tropical Pacific. The weak  
39 stochastic forcing in f3-L is insufficient to disrupt its overly intense ENSO cycle, yielding an overly  
40 regular oscillation. By identifying the structural sources of ENSO biases across resolutions, this study  
41 provides a reproducible and model-agnostic framework for diagnosing resolution effects on ENSO  
42 performance in climate models and informs future development of the FGOALS-f3 model family.

43

## 44 **1 Introduction**

45 El Niño-Southern Oscillation (ENSO), as one of the most prominent interannual variabilities in the  
46 Earth's climate system, exerts a profound influence on regional and global climate (McPhaden et al.,  
47 2006; Cai et al., 2021). Therefore, the ability to accurately simulate ENSO phenomenon serves as a  
48 fundamental benchmark for evaluating the fidelity of coupled climate models (Timmermann et al., 2018).  
49 Despite significant progress in the development of climate models, large inter-model spread remains in  
50 ENSO characteristics across Coupled Model Intercomparison Project (CMIP) generations (Zhang et al.,  
51 2020; Planton et al., 2021). Common biases include inaccuracies in simulating ENSO amplitude (Planton  
52 et al., 2021), period (Lu et al., 2018), seasonal phase locking (Liao et al., 2023; Yan and Sun, 2024),  
53 spatial distribution (Jiang et al., 2021), and intensity asymmetry (Zhao and Sun, 2022), as well as an  
54 overly regular ENSO oscillation (Chen et al., 2016a; Guilyardi et al., 2020). These deficiencies reflect  
55 systematic structural biases within models, which directly limit the predictive skill of dynamical models  
56 (Barnston et al., 2012) and hinder the reliability of climate projection regarding how ENSO may evolve  
57 under future climate change (Jiang et al., 2020a). Therefore, it is imperative to improve the fidelity of  
58 ENSO simulation in climate models.

59 Horizontal resolution has long been recognized as an important factor influencing model behavior  
60 (Yu et al., 2024). Motivated by this, the latest CMIP6 launched a dedicated High-Resolution Model Inter-  
61 comparison Project (HighResMIP) (Eyring et al., 2016) to systematically assess the benefits of increased  
62 resolution on model simulations. Previous studies have shown that as model resolution increases,  
63 simulation capabilities for both the climate mean state and variability exhibit improvements (Dawson et  
64 al., 2013; Chang et al., 2020). For example, high-resolution models demonstrate superior performance  
65 over low-resolution counterparts in simulating the Asian summer monsoon (He et al., 2025a), the impact  
66 of Tibetan Plateau thermal forcing on Asian summer monsoon (He et al., 2025b), the precipitation in  
67 southern China (Zi et al., 2024), the spatial distribution and frequency of tropical cyclones (Kreussler et  
68 al., 2021; Li et al., 2021), air-sea turbulent flux (Small et al., 2019), heat transport by boundary currents  
69 (Docquier et al., 2019), ocean mesoscale eddies (Hallberg, 2013), and Antarctic sea ice (Docquier et al.,  
70 2019). This is partly because higher resolution allows models to explicitly resolve finer-scale physical  
71 processes, reducing their dependence on parameterization schemes. Furthermore, high-resolution models  
72 facilitate a more accurate simulation of topographically sensitive regions, therefore improving the

73 simulation of atmosphere-ocean processes related to complex terrain (Bacmeister et al., 2014; Hewitt et  
74 al., 2016). Then a pertinent inquiry arises: does the ENSO simulation benefit from the increased  
75 resolution?

76       Regarding the impact of increased horizontal resolution on ENSO characteristics, previous studies  
77 found that when the atmospheric horizontal resolution in climate models was increased from 3.8° (T30)  
78 or 2.8° (T42) to 1° (T106), significant improvements can be found in the simulated ENSO period  
79 (Guilyardi et al., 2004; Navarra et al., 2008) and ENSO amplitude (Hua et al., 2018). However, the  
80 aforementioned studies were primarily based on the comparisons from ~400 km (or 300 km) to 100 km  
81 scales. In the latest climate models participated in the HighResMIP, model resolutions have advanced  
82 substantially, with some achieving 25 km resolution in atmospheric component and 10 km in oceanic  
83 component. This higher resolution enables a more realistic reproduction of climate variability, such as  
84 tropical cyclones (TCs) (Li et al., 2021) and tropical instability waves (Li et al., 2023). Yet, a critical  
85 question remains unresolved: when model resolution reaches ~25 km, a scale that can reasonably  
86 simulate weather-scale systems like TCs, does ENSO simulation also improve further?

87       ENSO is fundamentally driven by a number of coupled ocean-atmosphere feedbacks (Li, 1997; Jin  
88 et al., 2006; Chen et al., 2015b; Chen et al., 2016a); however, some analyses regarding ENSO simulations  
89 are often result-oriented, focusing only on changes in statistical indices while lacking sufficient  
90 diagnostic analysis of the key air-sea feedback processes that shape ENSO's properties. Therefore, it is  
91 necessary to conduct a process-oriented evaluation when comparing the ENSO simulation between  
92 different resolution versions.

93       It is worth noting that the observational evidences have suggested the significant influence of  
94 atmospheric "noise" on the development and evolution of ENSO (Chen et al., 2015a; Fedorov et al.,  
95 2015). Here the atmospheric "noise" primarily refers to high-frequency (HF) wind activities such as  
96 westerly wind bursts (Harrison and Vecchi, 1997; Fedorov, 2002), including synoptic and intra-seasonal  
97 scales. TC and Madden-Julian Oscillation (MJO; Madden and Julian, 1971; Madden and Julian, 1972)  
98 have been recognized as key sources of HF wind activities in recent studies (Ying et al., 2019; Liang and  
99 Fedorov, 2021). Considering the atmospheric components in HighResMIP models can reach a horizontal  
100 resolution of 50 km or finer (which is sufficient to reasonably reproduce TC features) and that the  
101 simulation performance for TC and MJO activities improves with increasing resolution (Davis, 2018;

102 Tang et al., 2022; Roberts et al., 2025), a further question arises: does the improved simulation of HF  
103 activities like TCs and MJO in high-resolution models contribute to improved ENSO simulation?

104 Motivated by these open questions, this study will conduct a process-oriented evaluation of ENSO  
105 simulation for a Chinese climate model, the Flexible Global Ocean–Atmosphere–Land System Finite-  
106 Volume version 3 (FGOALS-f3) climate system model that was developed by the Institute of  
107 Atmospheric Physics, Chinese Academy of Sciences (IAP-CAS). FGOALS-f3 participated in  
108 HighResMIP with both a low-resolution (~100 km; FGOALS-f3-L, hereafter f3-L) and a high-resolution  
109 version (~25 km; FGOALS-f3-H, hereafter f3-H) (An et al., 2022; Bao et al., 2020). The high-resolution  
110 version (f3-H) has been shown to have superior simulation performances over the low-resolution  
111 counterpart (f3-L) in representing mesoscale vortices (An et al., 2022), tropical instability waves (Li et  
112 al., 2023), TCs (Li et al., 2021), East Asian summer monsoon precipitation (Zi et al., 2024), and the  
113 climatological mean states (Yu et al., 2024). Therefore, this study employs the CAS-developed f3-H and  
114 f3-L to reveal the impact of model resolution on ENSO simulation performance and the underlying air-  
115 sea coupling processes.

116 This model evaluation study will provide insights into the resolution sensitivity of ENSO-related  
117 processes in FGOALS-f3 and establishes a diagnostic framework that can be applied to other coupled  
118 models participating in CMIP6 and future CMIP phases. The remainder of this paper is organized as  
119 follows. Section 2 describes the model configurations, observational datasets, and diagnostic framework.  
120 Section 3 presents an overview of the ENSO characteristics in two versions of FGOALS-f3 model.  
121 Section 4 and Section 5 demonstrate how the model horizontal resolution impacts the ENSO simulation.  
122 Section 6 summarizes the findings and discusses implications for model development and evaluation.

## 123 **2. Model configurations, datasets, and diagnostic framework**

### 124 **2.1 Model configurations**

125 FGOALS-f3 is a fully coupled climate system model developed by State Key Laboratory of  
126 Numerical Modeling for Atmospheric Sciences and Geophysical Fluid Dynamics (LASG), IAP-CAS,  
127 which couples four component models using the CPL7 coupler (Craig et al., 2012). The four component  
128 models are the atmospheric model FAMIL2.2 (He et al., 2019; Li et al., 2021), the ocean model  
129 LICOM3.0 (Li et al., 2020), the land model CLM4.0 (Lawrence et al., 2011), and the sea ice model

130 CICE4.0 (Hunke and Lipscomb, 2010).

131 The atmospheric component FAMIL2.2 is the last version of the Finite-volume Atmospheric Model  
132 developed by the LASG-IAP (FAMIL) (Li et al., 2021). FAMIL2.2 utilizes a finite-volume dynamical  
133 core constructed on a cubed sphere grid that is globally partitioned into six tiles (Zhou et al., 2015). In  
134 the vertical direction, the model uses hybrid coordinates over 32 layers, and the model top is 1 hPa. While  
135 the horizontal resolution ranges from C96 (about 100 km) to C384 (about 25 km) across the different  
136 resolution version. The oceanic component LICOM 3.0 is the third version of LASG-IAP Climate System  
137 Ocean Model (LICOM) (Yu et al., 2018). LICOM 3.0 updated a new advection scheme and employed a  
138 tripolar grid based on orthogonal curvilinear coordinates. The horizontal resolution of LICOM 3.0 can  
139 vary flexibly between  $1^\circ$  and  $1/20^\circ$ . Sub-grid parametrization schemes employed in LICOM 3.0 include  
140 the tidal mixing scheme, a buoyancy frequency related thickness diffusivity scheme, a vertical viscosity  
141 and diffusion scheme, and a chlorophyll-a dependent solar penetration scheme, etc. A comprehensive  
142 description of the physical package in LICOM3.0 can be found in Li et al. (2020). The land component  
143 in FGOALS-f3 model is Community Land Model (CLM) version 4.0. This advanced model simulates  
144 the water and momentum balances at the land surface and incorporates interactive carbon and nitrogen  
145 cycles, allowing for a more realistic representation of vegetation dynamics and ecosystem processes  
146 (Lawrence et al., 2011). In FGOALS-f3 model, sea ice is simulated using the Los Alamos Sea Ice Model  
147 version 4.0 (CICE 4.0). This is a dynamic-thermodynamic model that simulates the evolution of sea ice  
148 thickness, concentration, and velocity. It features multiple ice thickness categories and an elastic-viscous-  
149 plastic (EVP) rheology to model ice deformation and dynamics (Hunke and Lipscomb, 2010).

150 The FGOALS-f3 model includes two versions: f3-L and f3-H (He et al., 2019; An et al., 2022). Both  
151 models are participating in HighResMIP of CMIP6 and have successfully completed the Tier-1 and Tier-  
152 3 experiments. These two models have the same components and physical processes. The sole distinction  
153 between f3-H and f3-L lies in their horizontal resolution and the corresponding time steps within their  
154 finite-volume cubed-sphere dynamical core (FV3). To maintain the stability of the integration for the  
155 dynamical core, the two parameters ( $k\_split$  and  $n\_split$ ) in FV3 are set to 6 and 15 in f3-H, respectively  
156 (they are 2 and 6, respectively, in f3-L). The specific resolutions of each component of f3-L and f3-H  
157 models are shown in Table 1.

158

159 **Table 1.** Resolution comparison of each component model between the FGOALS-f3-L model and the FGOALS-f3-  
 160 H model

	FGOALS-f3-L	FGOALS-f3-H
Atmosphere	FAMIL2.2 (1°×1°, 32 levels)	FAMIL2.2 (0.25°×0.25°, 32 levels)
Ocean	LICOM3.0 (1°×1°, 30 levels)	LICOM3.0 (0.1°×0.1°, 55 levels)
Land	CLM4.0 (1.25°×0.9°)	CLM4.0 (0.31°×0.23°)
Sea Ice	CICE4.0 (1°×1°)	CICE4.0 (0.1°×0.1°)

161 The model data used in this study are obtained from the historical experiment outputs of f3-L and  
 162 f3-H model. Considering the experiment outputs of f3-H (highresSST-present) start from 1950, the period  
 163 during 1950-2014 for the two models are analyzed. The main variables used in this study include monthly  
 164 sea surface temperature (SST), three-dimensional ocean currents (uo, vo, wo), oceanic potential  
 165 temperature (thetao), surface wind stress (tauu, tauv), and net radiation flux (rsds, rsus, rlds, rlus, hfss,  
 166 hfls); daily surface wind (uas, vas), precipitation (pr), six-hourly sea level pressure (SLP), 850 hPa wind  
 167 (ua, va), 300 hPa and 500 hPa temperature (ta). All data is detrended before analyzing.

## 168 **2.2 Observation and reanalysis datasets**

169 The observational and reanalysis data used in this study include: 1) the monthly SST data obtained  
 170 from the Hadley Centre Sea Ice and Sea Surface Temperature version 1.1 dataset (HadISST v1,1), with  
 171 a horizontal resolution of 1°×1° (Rayner et al., 2003); 2) the monthly, daily, and hourly 10m wind fields  
 172 are from the European Centre for Medium-Range Weather Forecasts (ECMWF) reanalysis data Fifth  
 173 Generation (ERA5), with a horizontal resolution of 0.25°× 0.25° (Hersbach et al., 2020); 3) the daily  
 174 precipitation is from the Global Precipitation Climate Program version 1.3 (GPCP v1.3), with a  
 175 horizontal resolution of 2.5°× 2.5° (Adler et al., 2003); 4) the monthly sea surface wind stress data are  
 176 provided by the ECMWF Ocean Reanalysis Data (ORAS5), with a horizontal resolution of 1°× 1° (Zuo  
 177 et al., 2019) and America Ocean Data Assimilation Data Set version 2.2.4 (SODA v2.2.4), with a  
 178 horizontal resolution of 0.5°× 0.5° (Carton and Giese, 2008); 5) the historical TC data are from the China  
 179 Meteorological Administration (CMA) tropical cyclone best track dataset (Ying et al., 2014; Lu et al.,  
 180 2021).

## 181 **2.3 Diagnostic framework**

182 This study employs a reproducible, model-agnostic diagnostic framework for evaluating resolution-  
183 dependent ENSO behavior. Diagnostics include ENSO amplitude and spectrum, ENSO irregularity index,  
184 Bjerknes index diagnosis and the corresponding total derivative decomposition, meridional distribution  
185 index of zonal wind stress anomaly, oceanic zonal current decomposition, the HF atmospheric westerly  
186 (easterly) wind index and the corresponding noise-to-signal ratio, and TC detection and metrics.

187 Throughout this study, an overbar  $\overline{(\ )}$  denotes the climatological mean field, and a prime  $(\ )'$   
188 denotes the interannual anomaly obtained by removing the climatological seasonal cycle. The subscript  
189  $'HF'$  indicates a HF (sub-90-day) filtered field. For example,  $u'_{HF}$  denotes the HF component of daily  
190 zonal wind anomaly, obtained by applying a 90-day high-pass filter to the daily anomaly field. All  
191 symbols are used consistently throughout the paper unless otherwise specified.

### 192 **2.3.1 ENSO amplitude, spectral analysis and ENSO irregularity index (CVT)**

193 Monthly SSTA is computed after removing the climatological seasonal cycle. ENSO amplitude is  
194 measured by the standard deviation of Niño3.4 index (monthly SSTA averaged in 5°S–5°N, 170°–  
195 120°W). Power spectra are derived using the multi-taper method following Thomson (1982). To  
196 quantitatively evaluate the regularity of ENSO oscillation, we propose an ENSO irregularity index  
197 based on the coefficient of variation of inter-event time intervals (CVT). This metric is computed  
198 through the following steps.

199 First, ENSO events are identified using the 3-month running mean of the Niño3.4 index. A  
200 warm (cold) event is defined when the 3-month running mean Niño3.4 index exceeds 0.5 (falls  
201 below  $-0.5$ ) standard deviation of the Niño3.4 index, and the event is considered to terminate when  
202 the Niño3.4 index returns to within the  $\pm 0.5$  standard deviation range for at two consecutive months.

203 Second, the time interval between two successive events of the same sign is defined as the time  
204 separation between adjacent event peaks (i.e., the month of maximum warming for warm events or  
205 maximum cooling for cold events).

206 Third, the CVT is computed as the ratio of the standard deviation to the mean of these inter-  
207 event intervals:

$$208 \quad CVT = \frac{\sigma_T}{\mu_T} \quad (1),$$

209 where  $T$  denotes the set of all inter-event intervals, and  $\mu_T$  and  $\sigma_T$  denote the mean and the  
 210 standard deviation of these intervals, respectively.

211 Finally, the CVT is calculate separately for warm events ( $CVT_{warm}$ ) and cold events ( $CVT_{cold}$ ),  
 212 and their average is taken as the final ENSO irregularity index used in this study. A larger  $CVT$   
 213 indicates more irregular ENSO oscillation with highly variable inter-event spacing, whereas a  
 214 smaller  $CVT$  (approaching zero) indicates a more periodic and regular oscillation.

### 215 2.3.2 Bjerknes index diagnosis

216 In order to quantitatively analyze the air-sea coupling processes responsible for ENSO amplitude in  
 217 FGOALS-f3 models, the diagnostic framework of BJ index (Kim and Jin, 2011a, 2011b) is performed in  
 218 this study. The specific formulation is listed as follows:

$$219 \quad BJ = \frac{R-\varepsilon}{2} \quad (2),$$

$$220 \quad R = -\left(a_1 \frac{\langle \Delta \bar{u} \rangle_E}{L_x} + a_2 \frac{\langle \Delta \bar{v} \rangle_E}{L_y}\right) - \alpha_s + \mu_a \beta_u \langle -\frac{\partial \bar{T}}{\partial x} \rangle_E + \mu_a \beta_w \langle -\frac{\partial \bar{T}}{\partial z} \rangle_E + \mu_a \beta_h a_h \langle \frac{\bar{w}}{H_1} \rangle_E \quad (3),$$

$$221 \quad \frac{\partial \langle h' \rangle_w}{\partial t} = -\varepsilon \langle h' \rangle_w - F[\tau_x'] \quad (4),$$

$$222 \quad \langle Q' \rangle_E = -\alpha_s \langle T' \rangle_E \quad (5),$$

$$223 \quad \langle H(\bar{w})T_{sub}' \rangle_E = a_h \langle T' \rangle_E \quad (6),$$

$$224 \quad \langle h' \rangle_E - \langle h' \rangle_w = \beta_h [\tau_x'] \quad (7),$$

$$225 \quad \langle H(\bar{w})w' \rangle_E = \beta_w [\tau_x'] \quad (8),$$

$$226 \quad \langle u' \rangle_E = \beta_u [\tau_x'] + \beta_{uh} \langle h' \rangle_w \quad (9),$$

$$227 \quad [\tau_x'] = \mu_a \langle T' \rangle_E \quad (10),$$

228 where  $u$ ,  $v$ , and  $w$  are the three dimensional oceanic current velocity;  $T$  denotes sea surface temperature  
 229 ( $^{\circ}\text{C}$ );  $\langle \rangle_E$  and  $\langle \rangle_w$  represent averaged volume of the eastern box region ( $5^{\circ}\text{S}$ – $5^{\circ}\text{N}$ ,  $170^{\circ}$ – $90^{\circ}\text{W}$ ) and  
 230 western box region ( $5^{\circ}\text{S}$ – $5^{\circ}\text{N}$ ,  $130^{\circ}\text{E}$ – $170^{\circ}\text{W}$ ), respectively, from the ocean surface to the mixed layer  
 231 depth;  $L_x$  and  $L_y$  denote the longitudinal and latitudinal lengths of the eastern box, respectively;  $H_1$   
 232 denotes the mixed layer depth (two complementary strategies for specifying  $H_1$  are adopted in this study  
 233 and their results are compared in Section 4.1). The coefficients  $a_1$  and  $a_2$  are obtained through linear  
 234 regression using SST anomalies (SSTA) zonally or meridionally averaged at the boundaries and area-  
 235 averaged SSTA over the box. the " $\Delta$ " in equation (2) represents the differences of ocean current between

236 the eastern and western boundaries.  $H(\bar{W}) = \begin{cases} 1, & \bar{W} > 0 \\ 0, & \bar{W} \leq 0 \end{cases}$  is the step function to make sure only upward  
237 vertical motion is taken into account. Here, the Equation (1) defines the BJ index, serving as the primary  
238 metric for the growth rate examined in this analysis. The corresponding dynamic and thermodynamic  
239 feedbacks are expressed in Equation (2). In equation (3), the first term on the right-hand side is the  
240 damping process at the rate of  $\varepsilon$ ; the second term represents the Sverdrup transport across the equatorial  
241 Pacific basin. In Equations (4) to (9),  $\alpha_s$  ( $s^{-1}$ ) indicates the response of the thermodynamic damping to  
242 SSTA;  $\mu_a$  ( $N\ m^{-2}\ K^{-1}$ ) represents the response of surface wind stress anomalies ( $\tau_x'$ ) to SSTA;  $\beta_u$  ( $m\ s^{-1}$   
243  $(N\ m^{-2})^{-1}$ ) represents the response of upper ocean current anomalies ( $u_o'$ ) to  $\tau_x'$ ;  $\beta_h$  ( $m\ (N\ m^{-2})^{-1}$ )  
244 indicates the response of the anomalous zonal slope of the equatorial Pacific thermocline to  $\tau_x'$ ;  $\beta_w$  ( $m$   
245  $s^{-1}\ (N\ m^{-2})^{-1}$ ) denotes the response of ocean upwelling anomalies ( $w_o'$ ) to  $\tau_x'$ ;  $a_h$  ( $K\ m^{-1}$ ) shows the  
246 effect of thermocline depth change on subsurface temperature anomalies.

247 Based on the above equations, the main contributing terms of the BJ index include two negative  
248 feedback processes: the dynamic damping by mean advection (MA;  $-\left(a_1 \frac{\langle \Delta \bar{u} \rangle_E}{L_x} + a_2 \frac{\langle \Delta \bar{v} \rangle_E}{L_y}\right)$ ), the  
249 thermodynamic feedback (TD;  $-\alpha_s$ ), and three positive feedback processes: the zonal advection  
250 feedback (ZA;  $\mu_a \beta_u \langle -\frac{\partial \bar{T}}{\partial x} \rangle_E$ ), the thermocline feedback (TH;  $\mu_a \beta_h a_h \langle \frac{\bar{w}}{H_1} \rangle_E$ ), and the Ekman feedback  
251 (EK;  $\mu_a \beta_w \langle -\frac{\partial \bar{T}}{\partial z} \rangle_E$ ).

### 252 2.3.3 Meridional distribution index

253 To further quantify the meridional structure of ENSO-related  $\tau_x'$ , a meridional distribution index  
254 (MDI) that was proposed by Chen et al. (2015b), is employed. The MDI is defined as:

$$255 \quad MDI = \frac{\int_{-10^\circ}^{10^\circ} \tau_x'(y) |y| dy}{\int_{-10^\circ}^{10^\circ} \tau_x'(y) dy} \quad (11),$$

256 where  $y$  denotes latitude, and  $\tau_x'(y)$  represents the meridional profile of the normalized  $\tau_x'$ . The  
257 normalized  $\tau_x'$  obtained by regressing the zonal wind stress anomaly field onto the Niño4 region (5°S–  
258 5°N, 160°E–150°W) averaged zonal wind stress anomalies and then averaged over the Niño4 longitude  
259 range (160°E–150°W). The MDI provides a quantitative measure of the meridional concentration of  
260 ENSO-related  $\tau_x'$  within the equatorial band. Specifically, a smaller MDI indicates that  $\tau_x'$  is more  
261 concentrated near the equator, whereas a larger MDI indicates a broader meridional distribution.

### 262 2.3.4 Oceanic zonal current decomposition

263 ENSO-related zonal current anomaly ( $u'_o$ ) in the equatorial region is composed of anomalous  
 264 zonal geostrophic currents ( $u'_g$ ) and anomalous Ekman currents ( $u'_e$ ) (Su et al., 2010; Su et al., 2014).  
 265 The specific formulas of  $u'_g$  and  $u'_e$  are listed below:

$$266 \quad u'_g = -\frac{g\partial^2 D'}{\beta\partial y^2} \quad (12),$$

$$267 \quad u'_e = \frac{1}{\rho H_1} \frac{r_s \tau'_x + \beta y \tau'_y}{r_s^2 + (\beta y)^2} \quad (13),$$

268 where  $\beta$  and  $r_s$  are the planetary vorticity gradient and Rayleigh dissipation rate ( $0.5 \text{ day}^{-1}$ ),  
 269 respectively;  $\tau'_y$  denotes the sea meridional wind stress anomaly;  $H_1$  denotes the mean mixed layer  
 270 depth, and  $\rho$  is the seawater density.

### 271 2.3.5 HF westerly (easterly) wind index and noise-to-signal ratio

272 An index regarding the HF zonal wind anomalies is used to quantitatively measure the intensity of  
 273 HF westerly (easterly) wind activity in the f3-L and f3-H models. This index (named WWI index and  
 274 EWI index) is defined as the integration of the averaged zonal HF westerly (easterly) wind over a fixed  
 275 region ( $5^\circ\text{S}$ – $5^\circ\text{N}$ ,  $120^\circ\text{E}$ – $180^\circ$ ). The formula is as follows:

$$276 \quad WWI \text{ index} = \int_{time1}^{time2} u_{HF}' dt, \quad u_{HF}' > 1m/s \quad (14),$$

$$277 \quad EWI \text{ index} = \int_{time1}^{time2} u_{HF}' dt, \quad u_{HF}' < -1m/s \quad (15),$$

278 where  $u_{HF}'$  represents the daily zonal wind anomaly after applying a 90-day high-pass filter, *time1* and  
 279 *time2* represent the start and end time of the integrated period, respectively. In this study, the development  
 280 period of ENSO event (January to August) is selected as the integrated period.

281 A noise-to-signal ratio (*NSR*) metric is proposed to quantify the relative magnitude of stochastic  
 282 atmospheric forcing compared to the ENSO signal. The *NSR* is defined as:

$$283 \quad NSR = \frac{\sigma(u'_{HF})}{\sigma(SSTA_{Ni\tilde{n}o3.4})} \quad (16),$$

284 where  $\sigma(u'_{HF})$  is the standard deviation of 90-day high-pass-filtered zonal wind anomalies averaged over  
 285 the western equatorial Pacific ( $5^\circ\text{S}$ – $5^\circ\text{N}$ ,  $120^\circ\text{E}$ – $180^\circ$ ), and  $\sigma(SSTA_{Ni\tilde{n}o3.4})$  denotes the standard deviation  
 286 of Niño3.4 index. A larger *NSR* indicates stronger stochastic forcing relative to the ENSO signal, and  
 287 vice versa.

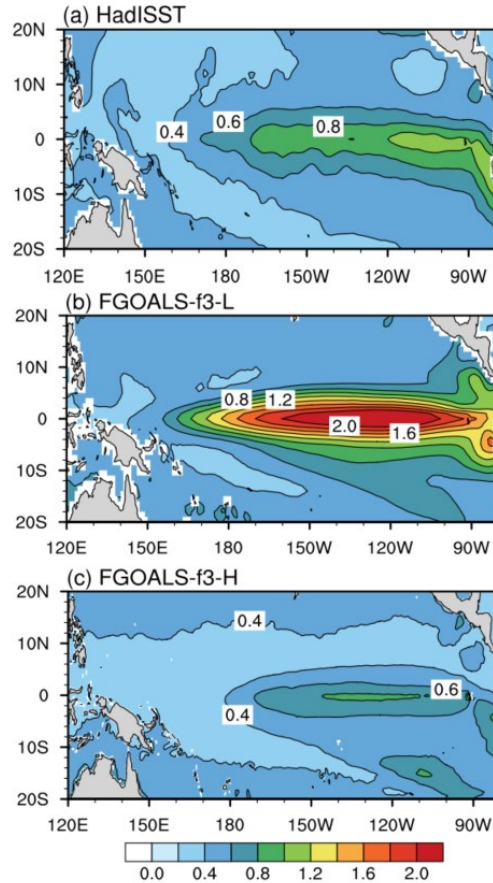
### 288 2.3.6 TC detection and metrics

289 The TC detection algorithm developed by the Geophysical Fluid Dynamics Laboratory  
290 (<https://www.gfdl.noaa.gov/tstorms/>; Zhao et al., 2023) was used to detect TC activities in FGOALS-f3  
291 model. The basic identification criteria and steps are: 1) a local minimum SLP is found within a maximum  
292 distance of 3,000 km; 2) the wind speed at 850 hPa for this vortex exceed 17 m/s; 3) the absolute value  
293 of the vorticity is greater than  $1.5 \times 10^{-4} \text{ s}^{-1}$ ; 4) The temperature within 1200 km of the vortex center is  
294 higher than that in the 1200-2400 km radius at 300-500 hPa, indicating a warm core structure; 5) The  
295 lifespan of this TC should be at least three days (72h).

296 We further employ two metrics, i.e, accumulated cyclone energy (ACE) and TC track density  
297 (TCTD), to assess the TC activity in FGOALS-f3 models. The ACE index (Bell et al., 2000) in each grid  
298 cell is defined as the sum of the squares of the maximum surface wind speeds for all TCs occurring within  
299 a  $4^\circ \times 4^\circ$  grid cell over all 6-hourly periods (i.e.,  $ACE = \sum_i V_{max}^2$ , where  $i$  denotes the  $i$ th TC in a grid cell  
300 and  $V_{max}$  denotes its maximum surface wind speed). The TCTD in each grid is defined as the sum of the  
301 number of TCs that have passed through the region within a distance of  $4^\circ \times 4^\circ$  from the grid center.

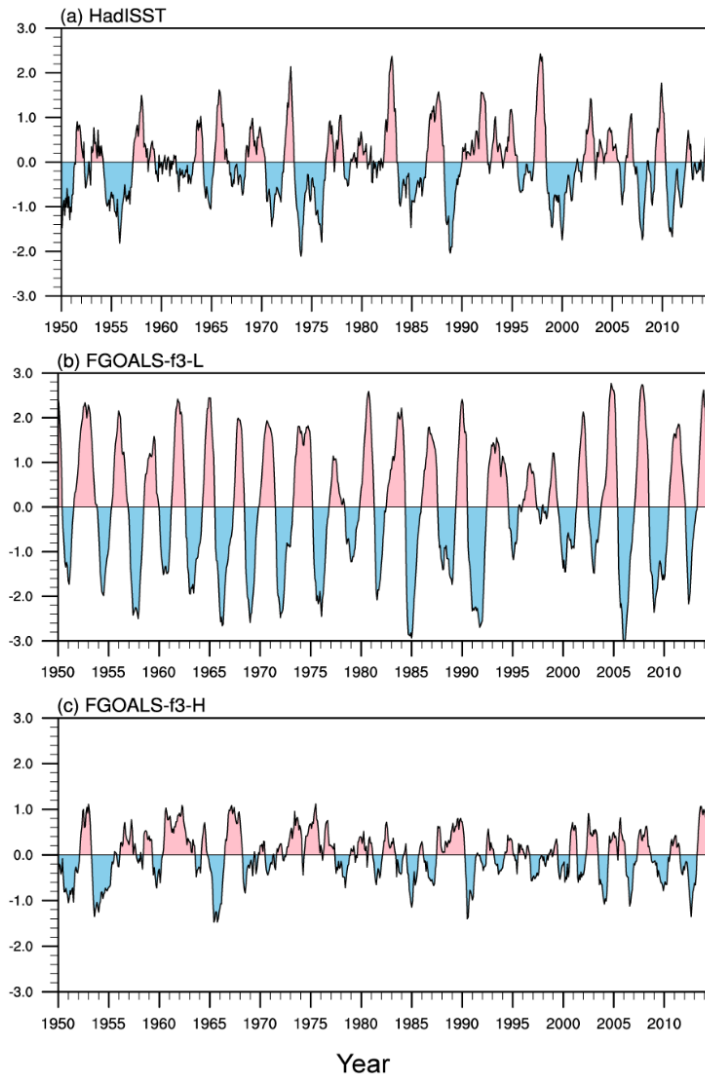
### 302 3. Evaluation of ENSO Characteristics in f3-L and f3-H

303 Figure 1 shows the spatial distribution of the standard deviation (STD) of SSTA over the tropical  
304 Pacific. In both the high- and low-resolution versions of FGOALS-f3, the interannual variability of SSTA  
305 is concentrated in the central-eastern equatorial Pacific (Fig. 1b-c), which is spatially consistent with the  
306 observation (Fig. 1a). However, significant differences exist in the ENSO amplitude. Specifically, the  
307 STD of the Niño3.4 index is  $0.79^\circ\text{C}$  in the observation,  $1.53^\circ\text{C}$  in f3-L, and  $0.62^\circ\text{C}$  in f3-H, respectively.  
308 This indicates that f3-L severely overestimates the ENSO amplitude, whereas f3-H's simulation is much  
309 closer to the observation. Considering that the ENSO amplitude simulated in f3-L is approximately 2.5  
310 times that of f3-H, this study will firstly address the causes of the stronger ENSO amplitude in f3-L  
311 compared to its counterpart in f3-H.



313 **Figure 1.** The standard deviation of SSTA (shading, units: °C) for (a) Observation (HadISST), (b) f3-L and (c) f3-  
 314 H.

315 Figure 2 presents the time series of the Niño3.4 index for the observation and the two model versions.  
 316 Obviously, the oscillation intensity of Niño3.4 index in f3-L is much stronger than that in the observation  
 317 and f3-H, consistent with the results of the STD analysis (Fig. 1). Another notable difference lies in the  
 318 regularity of the oscillation: ENSO events in f3-L exhibit highly periodic behavior, with a regular  
 319 transition between warm and cold phases. In contrast, the ENSO evolution in both the observation and  
 320 f3-H exhibit obvious irregularity. Furthermore, we conduct the power spectrum analysis on the Niño3.4  
 321 indices (Fig. 3). In the observation, the power spectrum is characterized by a broad band of 2–8 years.  
 322 However, the power spectrum in f3-L shows a sharp and significant unimodal peak at approximately 3-  
 323 year period, with excessive concentration of ENSO energy at this dominant period. In contrast, f3-H  
 324 reproduces a broadband spectral distribution similar to the observation.



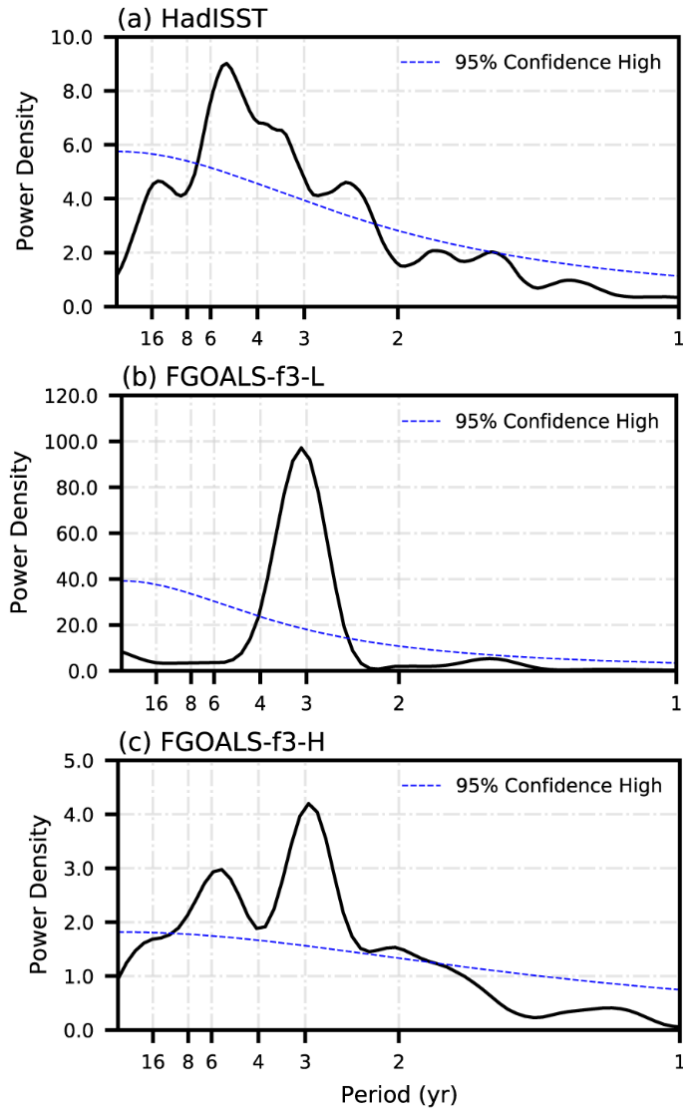
326 **Figure 2.** Temporal evolution of Niño3.4 index (the averaged SSTA in the Pacific Niño3.4 region (5°S–5°N, 170°W–  
 327 120°W), units: °C) for (a) Observation (HadISST), (b) f3-L and (c) f3-H.

328 Based on the proposed ENSO irregularity index, we calculated the *CVT* for the observation, f3-L  
 329 and f3-H. As shown in Table 2, the *CVT* values are 0.61, 0.17, and 0.53 for the observation, f3-L and f3-  
 330 H, respectively. The results clearly indicate that ENSO oscillation in f3-L is excessively regular compared  
 331 to the observation (*CVT* of 0.17 vs. 0.61), whereas f3-H produces a degree of irregularity much closes to  
 332 the observation. Therefore, the second question this study will address is: what causes the overly regular  
 333 oscillation in f3-L, while f3-H captures more realistic irregularity?

334 Table 2. The ENSO irregularity index (*CVT*) for the observation, f3-L and f3-H.

	<b>Observation</b>	<b>f3-L</b>	<b>f3-H</b>
<i>CVT</i>	0.61	0.17	0.53

335



337 **Figure 3.** The power spectra of Niño3.4 index for (a) Observation (HadISST), (b) f3-L and (c) f3-H. The blue line  
 338 in the plots is the 95% confidence level.

#### 339 **4. Process-based Diagnosis of ENSO Amplitude Differences**

##### 340 **4.1 Diagnostic analysis based on the BJ index**

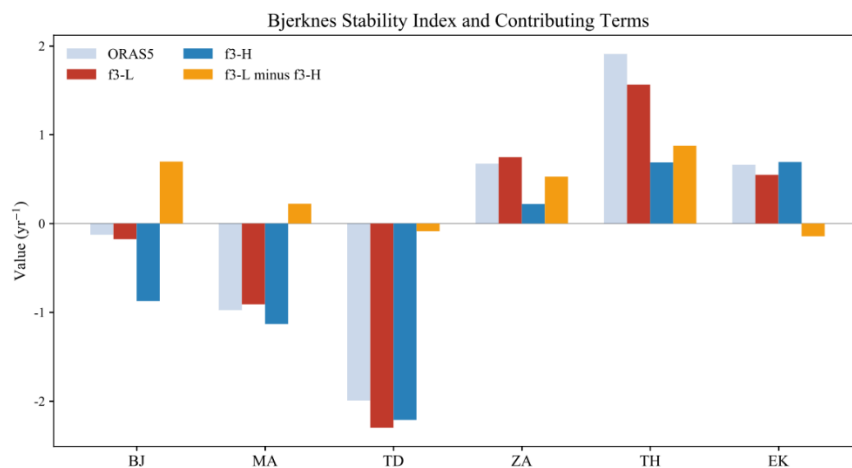
341 To investigate the physical mechanisms responsible for the ENSO amplitude difference between the  
 342 high- and low-resolution versions, we apply the BJ index framework to quantitatively diagnose the  
 343 stability of the coupled ocean-atmosphere system in both models. When applying the BJ index or the  
 344 commonly used mixed-layer heat budget diagnosis, one practical issue is the choice of mixed layer depth  
 345 (MLD) and whether the results are sensitive to this choice. We therefore first examine the spatial  
 346 distribution of the climatological MLD in f3-L and f3-H. Here the MLD is defined as the depth at which  
 347 the ocean temperature is 0.8°C lower than the SST, following Wang et al. (2012) and Chen et al. (2016b).  
 348 As shown in Figure S1, the climatological MLD exhibits a pronounced zonal variation along the  
 349 equatorial Pacific: it is relatively shallow in the far eastern Pacific and gradually deepens toward the

350 central equatorial Pacific. Moreover, the MLD differs between the two model versions, with the eastern  
 351 box-mean values of approximately 65 m in f3-L and 50 m in f3-H over the eastern equatorial Pacific (i.e.,  
 352 the eastern box used in the BJ index calculation). Given this zonal and inter-model variability, we adopt  
 353 two complementary MLD strategies in the BJ index diagnostic.

354 **Strategy 1 (Constant MLD):** A fixed MLD of a constant value is applied to both f3-L and f3-H  
 355 when computing the BJ index. This approach follows the conventional practice in previous BJ index  
 356 studies (e.g., Kim and Jin, 2011a, 2011b; Chen et al., 2019a, 2019b) and facilitates a direct comparison  
 357 between the two simulations under an identical diagnostic framework. From the perspective of the BJ-  
 358 index eastern-box average, the climatological mean MLD over the eastern equatorial Pacific is  
 359 approximately 65 m in f3-L and 50 m in f3-H. Therefore, in this first approach, we use a constant value  
 360 of 65 m for both simulations.

361 The BJ index results under Strategy 1 are shown in Figure 4. Figure 4 presents the BJ index  
 362 calculated using a fixed MLD of 65 m for the reanalysis, f3-L and f3-H, as well as their difference (f3-L  
 363 minus f3-H). The results demonstrate that, although both models yield negative BJ indices, the value for  
 364 f3-L is significantly larger (i.e., less negative) than that for f3-H. According to the physical interpretation  
 365 of the BJ index (Jin et al., 2006; Kim and Jin, 2011a; 2011b), the less negative BJ index in f3-L indicates  
 366 that the coupled air-sea system in f3-L is more unstable than that in f3-H. This more unstable coupled  
 367 system is more favorable for ENSO growth, thereby leading to a stronger ENSO amplitude in f3-L than  
 368 that in f3-H.

369



371 **Figure 4.** BJ index and the corresponding main contributing terms for the reanalysis (ORAS5; grey bars), f3-L (red  
 372 bars), f3-H (blue bars) and their difference (f3-L minus f3-H, orange bars). Here the BJ index is calculated using a  
 373 fixed MLD of 65 m. The five contributing terms include dynamic damping by mean advection (MA), thermodynamic  
 374 damping feedback (TD), zonal advection feedback (ZA), thermocline feedback (TH) and Ekman feedback (EK).

375 It is worth noting that the BJ index derived from the reanalysis is not more negative than that of f3-

376 L, despite the observed ENSO amplitude being slightly weaker than that simulated by f3-L. This  
377 inconsistency can be attributed to two factors. First, reanalysis products carry inherent uncertainties, and  
378 direct comparison between reanalysis-derived and model-derived BJ indices should be interpreted with  
379 caution. Second, the BJ index is a linear diagnostic framework that does not account for nonlinear  
380 processes, including nonlinear atmospheric responses, semi-stochastic atmospheric noise (i.e., the HF  
381 zonal wind anomalies discussed in this study), and oceanic nonlinear processes such as nonlinear  
382 dynamical heating (Wei et al., 2026). In other words, while the BJ index is a useful tool for assessing  
383 whether the linear air–sea coupling framework favors ENSO growth, the actual ENSO amplitude is  
384 jointly determined by linear coupling, nonlinear processes, and stochastic forcing. This represents an  
385 inherent limitation of the BJ index framework. Therefore, a comprehensive evaluation of ENSO  
386 simulation requires not only the BJ index analysis of linear feedback processes but also diagnostics  
387 beyond the linear framework to assess the roles of nonlinear processes and stochastic forcing, as  
388 addressed in Section 5 of this study. In the following, our primary focus is on examining the differences  
389 in the BJ index and its contributing terms between f3-L and f3-H.

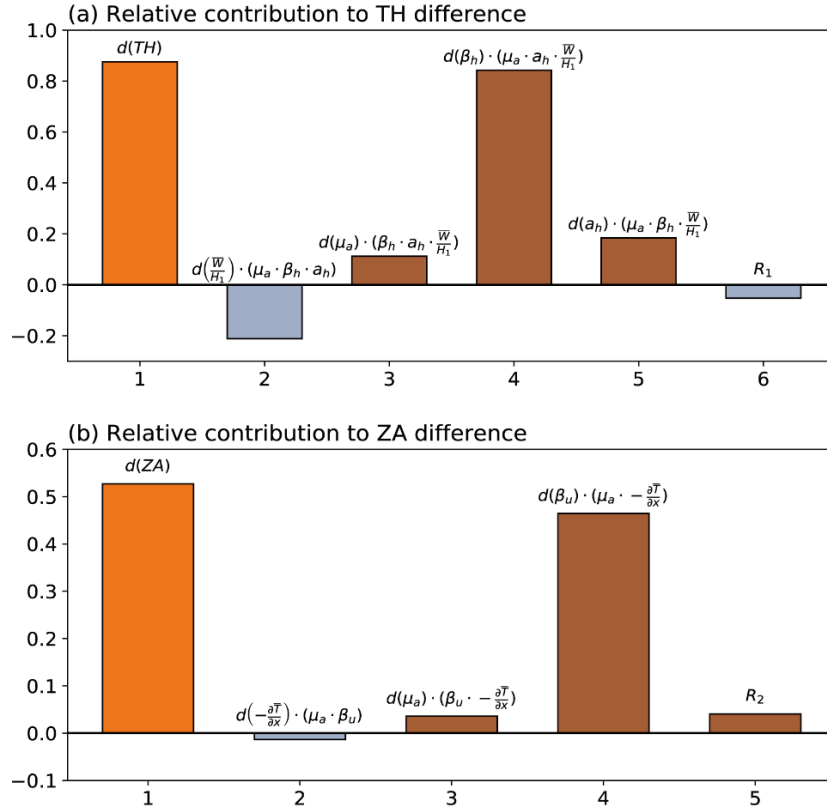
390 A further question arises: which physical processes contribute to the more unstable coupled system  
391 in f3-L? By examining the differences in the five contributing terms of the BJ index (orange bars in Fig.  
392 4), we find that the differences in the thermocline feedback (TH) term and the zonal advection feedback  
393 (ZA) term are the dominant contributors to the BJ index difference (i.e., the system stability) between  
394 the two model versions. Therefore, the subsequent analysis will focus on the physical mechanisms  
395 responsible for the stronger TH and ZA terms in f3-L relative to f3-H.

396 **Strategy 2 (Longitude-varying MLD):** Each model version uses its own longitude-dependent  
397 climatological MLD (averaged over the equatorial band, 5°S–5°N) when computing the BJ index. This  
398 approach accounts for zonal variations and inter-model differences in stratification, providing a more  
399 physically realistic diagnostic. In this approach, when calculating the BJ index, we diagnose the mixed-  
400 layer temperature anomaly above the longitudinally varying climatological MLD (Figure S1) within the  
401 three-dimensional eastern equatorial Pacific box.

402 Figure S2 presents the BJ index and its contributing terms calculated using the longitude-varying  
403 MLD for the reanalysis, f3-L, and f3-H, as well as their difference (f3-L minus f3-H). The main results  
404 are broadly consistent with those obtained under Strategy 1. Specifically, the BJ index of f3-H remains  
405 more negative than that of f3-L, which largely explains the weaker ENSO amplitude in f3-H; and the BJ  
406 index difference between the two models is still primarily attributable to the TH and ZA terms. The only

407 notable discrepancy between the two strategies lies in the MA term, which represents the dynamic  
408 damping by mean zonal and meridional advection. In brief, under the longitude-varying MLD strategy,  
409 the shallower MLD in f3-H means that the vertical averaging is taken over a thinner layer, in which the  
410 poleward (damping) branch dominates more strongly, resulting in a more negative MA term in f3-H  
411 compared to f3-L. A detailed analysis regarding the MA difference between f3-H and f3-L is provided in  
412 the supplementary material. Overall, the sensitivity test demonstrates that the core conclusions of the BJ  
413 index analysis, namely, the more unstable coupled system in f3-L and the dominant roles of the TH and  
414 ZA terms are robust across both MLD strategies.

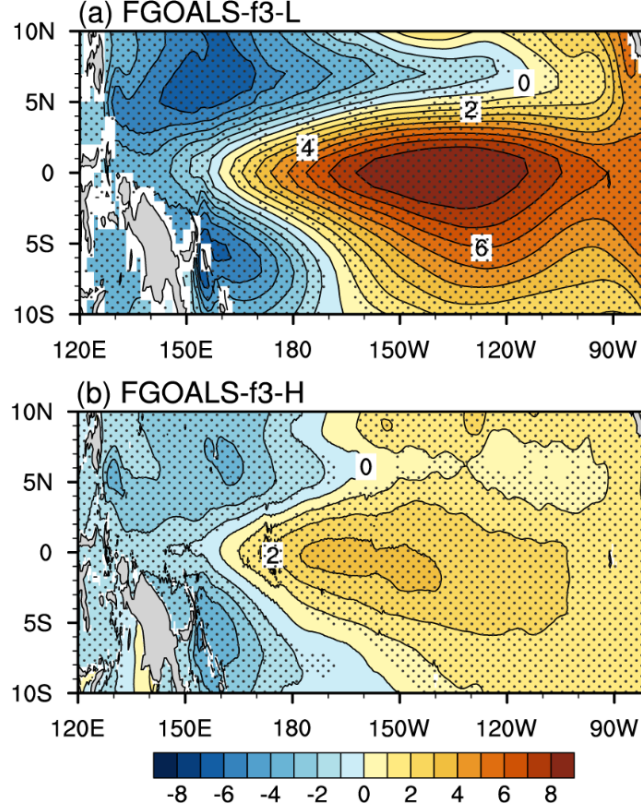
415       According to the definition of the BJ index (see Eq. (3)), each ocean dynamic term consists of two  
416 components: one related to the mean state and the other to air-sea feedback processes. Considering that  
417 both components may contribute to the differences in the TH and ZA terms between f3-L and f3-H, we  
418 calculate the relative contributions of each component to the total difference using a total derivative  
419 decomposition. As shown in Figure 5a, the stronger TH term in f3-L compared to f3-H (bar 1) primarily  
420 arises from the difference in  $\beta_h$  (bar 4). The differences in  $\mu_a$  and  $a_h$  make minor contributions, while  
421 the mean state differences and the covariance term make negative contributions. Thus, the dominant  
422 factor responsible for the stronger TH term in f3-L is the difference in  $\beta_h$ . Similarly, for the stronger ZA  
423 term in f3-L, the results (Fig. 5b) show that the difference in ZA term (bar 1) is primarily determined by  
424 the difference in  $\beta_u$  (bar 4), while the difference in  $a_h$  and the covariance term have marginal  
425 contributions.



427 **Figure 5.** (a) Contributions of different components to the change in TH term. Bar 1 indicates the change in TH term  
428 [f3-Lminus f3-H,  $d(TH)$ ]. Bar 2 denotes the contribution from the mean state part change [ $d(\bar{w}/H_1)$ ] to the change  
429 in TH term. Bar 3, 4 and 5 indicate the contributions from the air-sea feedbacks [ $d(\mu_a)$ ,  $d(\beta_h)$  and  $d(a_h)$ ] to the change  
430 in TH term, respectively. Bar 6 is the residual, which denotes the contribution from the covariant changes of both  
431 the mean state part and the air-sea feedbacks. (b) same as (a) but for the zonal advection feedback (ZA). Bar 1  
432 indicate the change in ZA term [f3-L minus f3-H,  $d(ZA)$ ]. Bar 2 denotes the contribution from the mean state part  
433 change [ $d(\partial \bar{T} / \partial x)$ ] to the change in ZA term. Bar 3 and Bar 4 indicate the contributions from the air-sea feedbacks  
434 [ $d(\mu_a)$  and  $d(\beta_u)$ ], respectively. Bar 5 is the residual, representing the contribution from the covariant changes of  
435 both the mean state part and the air-sea feedbacks.

#### 436 4.2 Resolution dependence of the $\beta_h$ feedback process difference

437 The air-sea feedback process  $\beta_h$  represents the response of the equatorial Pacific thermocline tilt  
438 to  $\tau_x'$ . Figure 6 shows the regression of thermocline depth anomalies onto zonal wind stress anomalies  
439 for the two models. Both models reproduce the expected pattern: in response to positive  $\tau_x'$  over the  
440 equatorial Pacific, the anomalous thermocline depth ( $D'$ ) deepens in the eastern equatorial Pacific and  
441 shoals in the western equatorial Pacific. However, the response is much stronger in f3-L than in f3-H.



443 **Figure 6.** Distribution of the response of thermocline depth anomaly to zonal wind stress anomaly [ $\beta_h$ ; units:  $\text{m} (\text{N}$   
 444  $\text{m}^{-2})^{-1}$ ] for (a) f3-L and (b) f3-H. Based on the linear relationship between sea surface height anomaly (SSHA) and  
 445 thermocline depth anomaly ( $D'$ ), the SSHA is used as a proxy of  $D'$ . The  $D'$  response to zonal wind stress anomaly  
 446 is derived through regressing the SSHA field onto the averaged zonal wind stress anomaly over equatorial Pacific  
 447 ( $5^{\circ}\text{S}$ – $5^{\circ}\text{N}$ ,  $120^{\circ}\text{E}$ – $100^{\circ}\text{W}$ ). The stippling in this plot denotes the regression coefficient exceeding a confidence level  
 448 of 99% by using Student's  $t$  test.

449 Based on the Sverdrup balance relationship (Jin, 1997; Li, 1997), the response of the  $D'$  to  $\tau_x'$  is  
 450 primarily determined by the mean equatorial thermocline depth ( $\bar{H}$ ) and  $\tau_x'$ :

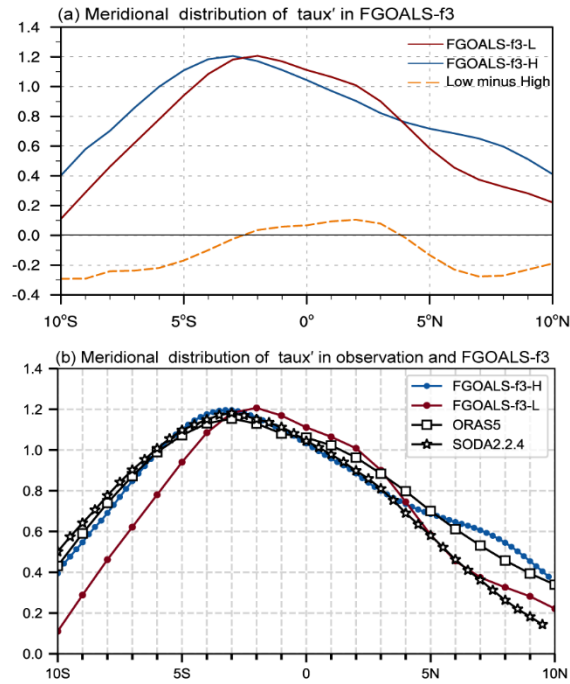
$$451 \quad \frac{\partial D'}{\partial x} = \frac{\tau_x'}{\rho g \bar{H}} \quad (17),$$

452 where  $\rho$  is the seawater density and  $g$  is the reduced gravity. We first examine the mean thermocline  
 453 depth in both models and find that the difference in  $\bar{H}$  between f3-L and f3-H is negligible (figure not  
 454 shown). Therefore, the difference in  $\bar{H}$  is not the primary cause.

455 Previous studies (Chen et al., 2015b; Chen et al., 2019a) have pointed out that the meridional  
 456 structure of  $\tau_x'$  is another key factor influencing the strength of  $\beta_h$ . Figure 7a presents the meridional  
 457 structure of  $\tau_x'$  for the two models and their difference (orange, f3-L minus f3-H). A significant  
 458 difference exists: although the regression results show the same magnitude of  $\tau_x'$  within the equatorial  
 459 Pacific ( $5^{\circ}\text{S}$ – $5^{\circ}\text{N}$ ), the  $\tau_x'$  in f3-L is meridionally more concentrated near the equator ( $0^{\circ}$ ) than that in

460 f3-H. Since the  $\tau_x'$  closer to equator is more effective in influencing  $D'$  (Chen et al., 2015b; Chen et al.,  
 461 2019a), this more equatorially-confined meridional structure of  $\tau_x'$  in f3-L inevitably results in a  
 462 stronger response of  $D'$  to  $\tau_x'$  (i.e., a larger  $\beta_h$ ).

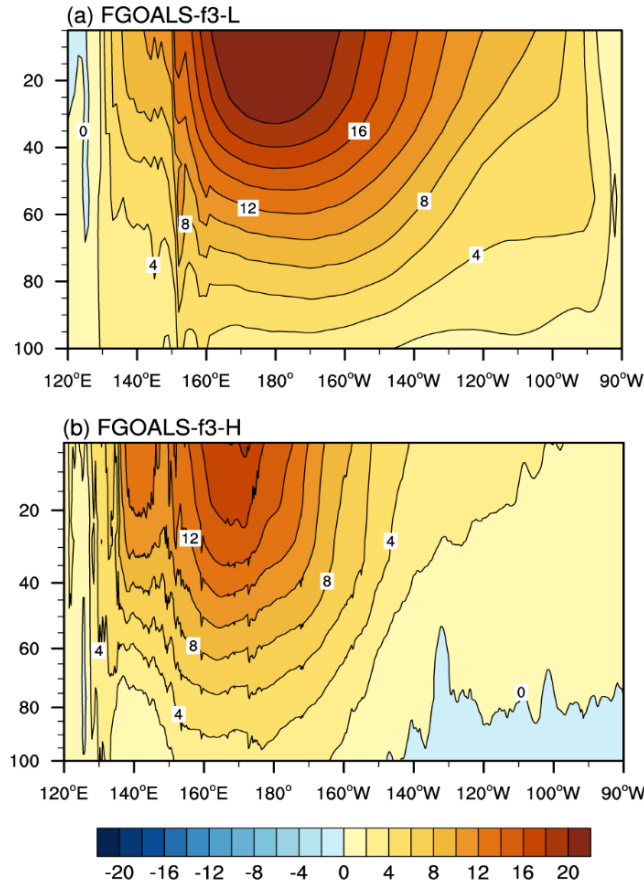
463 Furthermore, we compare the meridional structure of ENSO-related  $\tau_x'$  in the two model versions  
 464 with two reanalysis datasets. As shown in Fig. 7b, the meridional structures of  $\tau_x'$  in the two reanalysis  
 465 products (black lines) are very similar between 10°S–5°N, while some discrepancies exist within 5°N–  
 466 10°N region. For the models, the f3-H (25 km atmospheric resolution) shows a  $\tau_x'$  meridional structure  
 467 in the equatorial region (5°S–5°N) that substantially resembles both reanalysis datasets. In contrast, the  
 468 meridional structure of  $\tau_x'$  within 5°S–5°N in f3-L (100 km atmospheric resolution) shows obvious  
 469 discrepancies from the two reanalysis datasets. This suggests that model horizontal resolution can  
 470 influence ENSO simulation by affecting the meridional distribution of  $\tau_x'$ . The higher horizontal  
 471 resolution is conducive to the more realistic representation of equatorial  $\tau_x'$  meridional structure,  
 472 thereby yielding a more reasonable thermocline feedback and ENSO amplitude.



474 **Figure 7.** Meridional structure of normalized zonal wind stress anomalies [units:  $\text{N m}^{-2} (\text{N m}^{-2})^{-1}$ ] averaged over the  
 475 Niño4 longitude range (160°E–150°W) for (a) the result of f3-L (red solid line), f3-H (blue solid line) and their  
 476 difference (orange dash line, f3-L minus f3-H). In this plot, all the data are both interpolated onto a  $1^\circ \times 1^\circ$  grid to  
 477 facilitate the comparison; (b) the results of ORAS5 (black line marked by square, with a  $1^\circ \times 1^\circ$  grid), SODA2,2,4  
 478 (black line marked by asterisk, with a  $0.25^\circ \times 0.25^\circ$  grid), f3-L (red line marked by circle, with a  $1^\circ \times 1^\circ$  grid) and  
 479 f3-H (blue line marked by circle, with a  $0.25^\circ \times 0.25^\circ$  grid). The normalized zonal wind stress anomalies are obtained  
 480 by regressing the zonal wind stress anomalies field onto the Niño4 region (5°S–5°N, 160°E–150°W) averaged zonal  
 481 wind stress anomalies.

482 **4.3 Resolution dependence of the  $\beta_u$  feedback process**

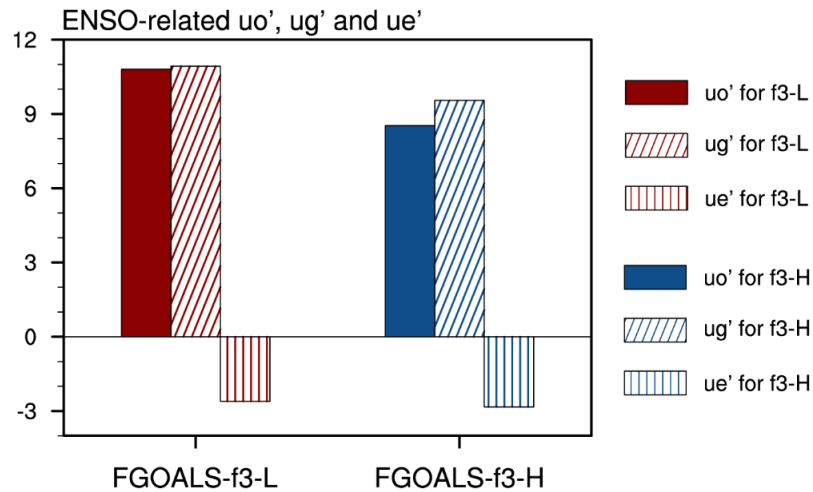
483 The air-sea feedback process  $\beta_u$  represents the response of the equatorial Pacific upper ocean zonal  
 484 current anomaly ( $u'_o$ ) to  $\tau'_x$ . Figure 8 shows the equatorial profile for the response of  $u'_o$  to  $\tau'_x$  in both  
 485 models. Both models simulate eastward  $u'_o$  a unit eastward  $\tau'_x$  in equatorial Pacific, but the response  
 486 is significantly stronger in f3-L than in f3-H.



488 **Figure 8.** Vertical profile (averaged over 5°S–5°N) of the response of zonal ocean current anomaly ( $u'_o$ ) to the zonal  
 489 wind stress anomaly [ $\beta_u$ ; units:  $\text{m s}^{-1}$  ( $\text{N m}^{-2}$ )<sup>-1</sup>] for (a) f3-L and (b) f3-H. The  $u'_o$  response to zonal wind stress  
 490 anomaly is derived through regressing the  $u'_o$  field onto the averaged zonal wind stress anomaly over equatorial  
 491 Pacific (5°S–5°N, 120°E–100°W).

492 Considering that ENSO-related  $u'_o$  in the equatorial region is composed of anomalous zonal  
 493 geostrophic currents ( $u'_g$ ) and anomalous Ekman currents ( $u'_e$ ) (see Section 2.3.4), we first diagnose the  
 494 response of  $u'_g$  and  $u'_e$  to wind stress anomalies (Fig. 9). In both versions, the response of  $u'_o$  to  $\tau'_x$   
 495 is primarily contributed by the response of  $u'_g$  to  $\tau'_x$ , while the contribution of  $u'_e$  is much smaller.  
 496 This indicates that the difference in  $u'_g$  response to  $\tau'_x$  is the main cause of the difference in  $\beta_u$   
 497 between the two model versions. Based on the geostrophic formula (Eq. (12)), the magnitude of  $u'_g$  is  
 498 related to the second-order meridional derivative of  $D'$ . Since the meridional structure of  $D'$  (Figure 6)

499 exhibits a parabolic shape (peaking at equator and decreasing poleward), a stronger  $D'$  in the equatorial  
 500 region corresponds to a larger value of second-order meridional derivative ( $-\frac{\partial^2 D'}{\partial y^2}$ ) and, consequently, a  
 501 stronger  $u'_g$ . As the  $D'$  response to  $\tau'_x$  is primarily modulated by the  $\beta_{\bar{h}}$  process, the difference in the  $\beta_u$   
 502 between the f3-L and f3-H is also primarily attributed to difference in the  $\beta_{\bar{h}}$  process. That is, the  
 503 stronger  $\beta_{\bar{h}}$  in f3-L leads to a stronger  $D'$ , which in turn induces a stronger  $u'_g$  and  $u'_o$  and ultimately  
 504 resulting in a stronger  $\beta_u$ .

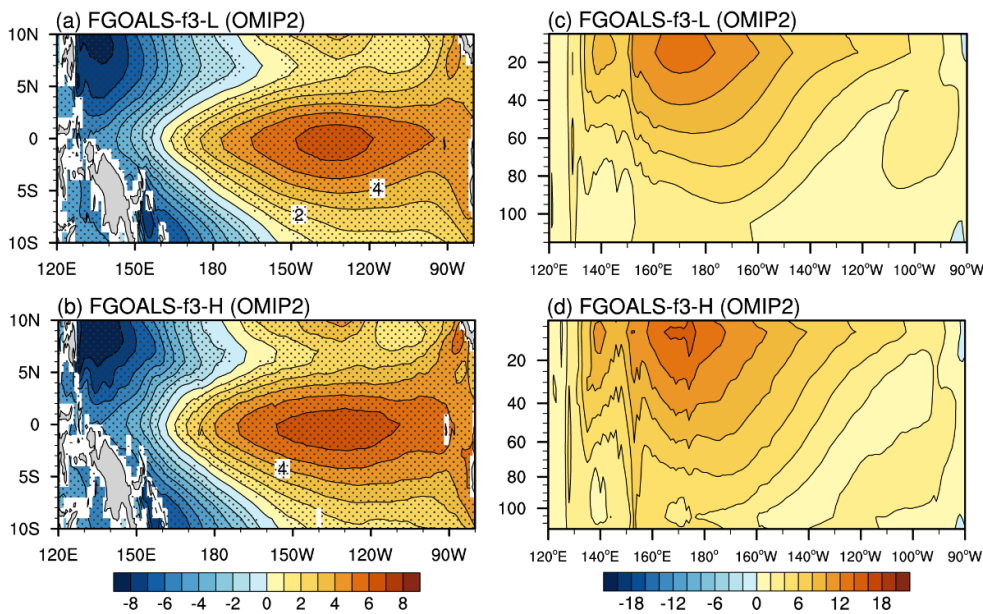


506 **Figure 9.** The ENSO-related zonal current anomalies ( $u'$ ) averaged over 0–65m, zonal geostrophic current anomalies  
 507 ( $u_g'$ ) and zonal Ekman current anomalies ( $u_e'$ ) along the equatorial eastern Pacific (2°S–2°N, 180°–80°W) for f3-L  
 508 (red bar) and f3-H (blue bar). The ENSO-related zonal current anomalies, zonal geostrophic current anomalies and  
 509 zonal Ekman current anomalies are obtained by regressing it anomalies field onto the zonal wind stress anomalies  
 510 averaged over Niño4 region (5°S–5°N, 160°E–150°W), respectively.

#### 511 4.4 Comparison with OMIP simulations

512 It should be noted that although our conclusions drawn from Coupled General Circulation Model  
 513 (CGCM) indicate that the improved ENSO simulation is closely linked to the increased atmospheric  
 514 resolution, the potential influence of oceanic horizontal resolution on ENSO simulation also merits brief  
 515 examination. For instance, from the perspective of the oceanic component of CGCM (OGCM), Li et al.  
 516 (2025) examined the oceanic zonal current and thermocline depth anomalies to zonal wind forcing by  
 517 analyzing the outputs from Ocean Model Intercomparison Project 2 (OMIP2, Griffies et al. 2016) and  
 518 found that the oceanic response to wind forcing is a key factor influencing ENSO simulation. Therefore,  
 519 the resolution-induced contrast between the OMIP experiment and the CMIP experiment (i.e., the  
 520 “historical” experiment) is a noteworthy phenomenon that warrants explanation.

521 According to the CMIP6’s protocol, OMIP2 experiments are forced by the identical atmospheric  
 522 reanalysis datasets, thus providing an ideal framework to isolate biases originating from the oceanic  
 523 component. Both f3-L and f3-H have participated in OMIP2, with respective oceanic horizontal  
 524 resolutions of approximately 1° and 0.1°. To further assess the potential impact of oceanic horizontal  
 525 resolution on ENSO simulation, we compare the key air-sea feedback terms ( $\beta_h$  and  $\beta_u$ ) between f3-L  
 526 and f3-H OMIP2 outputs. As shown in figure 10, the response of zonal current and thermocline depth  
 527 anomalies to the identical  $\tau_x'$  are remarkably similar between the two ocean models. This indicates that  
 528 the differences in OGCM resolution itself may not be the primary driver of the differences in  $\beta_h$  and  
 529  $\beta_u$ . Moreover, this finding (Fig. 10) stands in stark contrast to the large differences in  $\beta_h$  and  $\beta_u$   
 530 identified in the two coupled simulations (Figures 6 and 8).



532 **Figure 10.** (a)–(b) and (c)–(d) are same as Figure 6 and 8, respectively, but for the OMIP2 simulations.

533 To understand the contrasting OMIP–CMIP behavior, we compare the meridional structures of the  
 534 “normalized  $\tau_x'$ ” between the CMIP and OMIP experiments for both model versions, as shown in Figure  
 535 S5. Here the normalized  $\tau_x'$  is obtained by regressing the  $\tau_x'$  field onto Niño4-region-averaged  $\tau_x'$ ;  
 536 and then averaging over the Niño4 longitude range (160°E–150°W). This normalization procedure  
 537 enables a fair comparison of the meridional structure of  $\tau_x'$  across different experiments and model  
 538 versions. In f3-L, the CMIP experiment produces stronger  $\tau_x'$  near the equator compared to the OMIP  
 539 forcing that was derived from the JRA55-do reanalysis (red lines in Fig. S5). This leads to an enhanced  
 540 thermocline response in CMIP relative to OMIP. Conversely, in f3-H, the CMIP experiment yields

541 weaker equatorial  $\tau_x'$  than the OMIP forcing (blue lines in Fig. S5), resulting in a weaker thermocline  
 542 response in CMIP relative to OMIP.

543 Table 3. Meridional distribution index (MDI; units:  $^\circ$ ) of  $\tau_x'$ , calculated from the meridional  
 544 structure of normalized  $\tau_x'$  as shown in Fig. B6.

	<b>f3-L</b>	<b>f3-H</b>
CMIP	2.55	2.71
OMIP	2.68	2.64

545 Furthermore, we quantify these structural differences in  $\tau_x'$  between the CMIP and OMIP  
 546 experiments based on the *MDI* metric, as introduced in section 2.3.3. The qualitative differences in  $\tau_x'$   
 547 distributions shown in Fig. S5 are corroborated by the *MDI* results (Table 3). In f3-L, the CMIP  
 548 experiment yields a notably smaller *MDI* ( $2.55^\circ$ ) than the OMIP experiment ( $2.68^\circ$ ), indicating a more  
 549 equatorially concentrated  $\tau_x'$  structure that can more efficiently drive thermocline variability, and hence  
 550 produces a larger  $\beta_h$  in the CMIP experiment. Conversely, in f3-H, the CMIP experiment exhibits a larger  
 551 *MDI* ( $2.71^\circ$ ) than the OMIP experiment ( $2.64^\circ$ ), corresponding to a broader  $\tau_x'$  distribution that drives  
 552 a more moderate thermocline response and a smaller  $\beta_h$ .

553 Therefore, the evidence from the OMIP2 experiments corroborates our main conclusion: the refined  
 554 atmospheric horizontal resolution, which more realistically captures the meridional structure of  $\tau_x'$ , plays  
 555 a decisive role in improving the simulation of the key air-sea feedbacks ( $\beta_h$  and  $\beta_u$ ) and ENSO  
 556 amplitude in FGOALS-f3 model. Nevertheless, a more comprehensive investigation, potentially  
 557 involving finer oceanic resolutions and their interactions with the atmosphere, deserves further  
 558 exploration in the future.

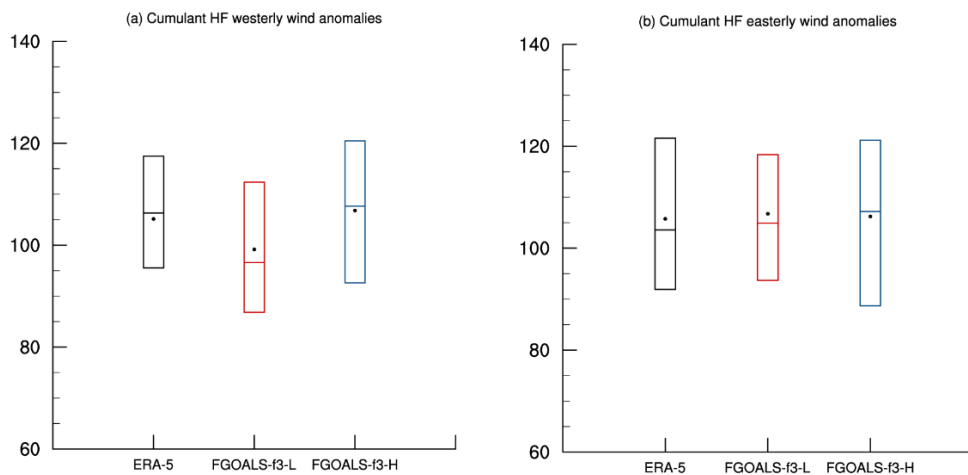
## 559 **5. Diagnostic of Oscillation Regularity**

### 560 **5.1 Resolution dependence of ENSO irregularity: Differences in HF wind activity**

561 A large body of studies have suggested that the HF zonal wind activity over the western and central  
 562 equatorial Pacific (WCEP) plays a crucial role in the onset and development of ENSO events (Rong et  
 563 al., 2011; Chen et al., 2017). In general, this HF zonal wind activity refers to westerly wind event (WWE)  
 564 and easterly wind event (EWE) with time scales less than 90 days. Due to their transient, intense, and  
 565 somewhat random nature, the HF zonal wind forcing is also considered as an important factor

566 contributing to the diversity and irregularity of ENSO (Chen et al., 2015a; Fedorov et al., 2015).  
 567 Motivated by this, we hypothesize that the difference in the ENSO regularity between f3-L and f3-H may  
 568 arise from the differences in HF zonal wind activity.

569 To test this, we calculate the intensity of the HF zonal wind activity based on the Equations (14) and  
 570 (15). Figure 11 shows the WWI and EWI index that measures the cumulative sum of HF westerly  
 571 (easterly) wind anomalies over WCEP during the ENSO development period, for the observation and the  
 572 two model versions. As shown in Figure 11a, the intensity of HF westerlies in f3-H is comparable to that  
 573 in the observation, with similar mean and median values. However, f3-L simulates much weaker intensity  
 574 of HF westerlies. For HF easterly activity (Fig. 11b), both models show comparable statistics to the  
 575 observation, with no significant differences between f3-L and f3-H. Overall, these results indicate that  
 576 f3-L strongly underestimates HF westerly wind activity relative to the f3-H and the observation.



578 **Figure 11.** The boxplots of the (a) WWI index and (b) EWI index during the ENSO development phase (January to  
 579 August). Red, blue and black boxes indicate the f3-L, f3-H and observations, respectively. The upper and lower  
 580 boundaries of the box represent the 75th and 25th percentile values, respectively. The horizontal line in the box  
 581 represents the median. The black dot represents the average value.

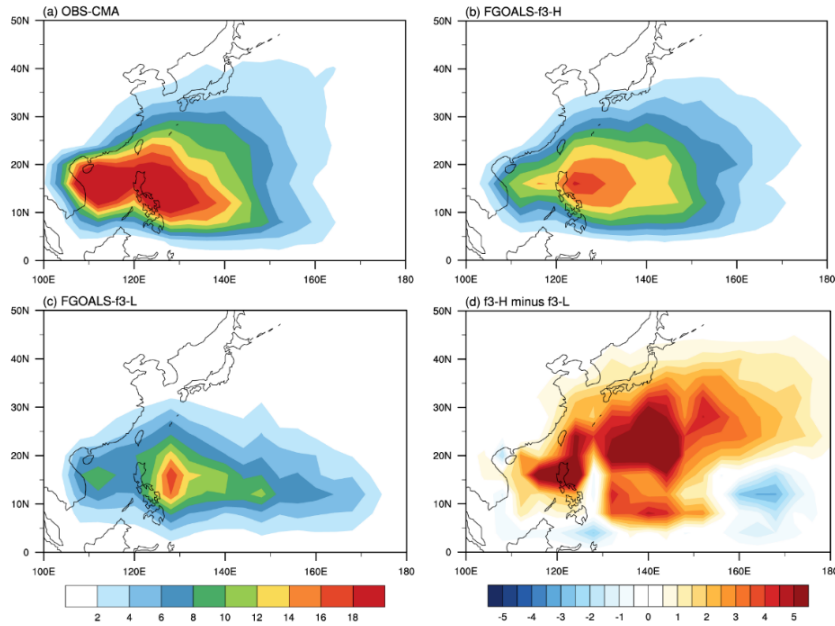
582 HF westerly wind activities are considered as semi-stochastic perturbations that modulate ENSO  
 583 evolution (Gebbie et al., 2007; Gebbie and Tziperman, 2009). On the one hand, their occurrence is partly  
 584 influenced by ENSO-related SSTA (Sun et al., 2020), but is also regarded as random noise independent  
 585 of ENSO system (Moore and Kleeman, 1999). Most ENSO theoretical models treat HF westerly wind  
 586 activity as external white noise forcing (Eisenman et al., 2005). This implies that the impact of HF activity  
 587 on the coupled system depends, to some extent, on its relative magnitude relative to the ENSO amplitude.  
 588 Notably, the aforementioned analysis based on the BJ index (a linear framework that excludes nonlinear

589 processes like atmospheric "noise") has shown that the coupled system simulated by f3-L is more  
590 unstable than that of f3-H, hence the ENSO variability in f3-L is more prone to self-sustained oscillation.  
591 Considering that the HF wind activities in f3-L is also significantly weaker than that in f3-H, from the  
592 perspective of signal-to-noise ratio, this weaker "noise" is insufficient to "disrupt" the overly strong  
593 ENSO oscillation in f3-L, allowing its ENSO cycle to evolve in a regular and self-sustained manner.

594 To further quantify the relative magnitude of stochastic atmospheric forcing compared to the ENSO  
595 signal, we introduce an *NSR* metric, as introduced in section 2.3.5. A larger *NSR* indicates stronger  
596 stochastic forcing relative to the ENSO signal. The *NSR* values are 2.67, 1.98, and 4.73 ( $\text{m s}^{-1} \text{K}^{-1}$ ) for  
597 the observation, f3-L, and f3-H, respectively. The substantially smaller *NSR* in f3-L reflects the  
598 combination of its weaker HF wind activity and stronger ENSO amplitude, confirming that the stochastic  
599 forcing in f3-L is insufficient to disrupt its overly intense ENSO oscillation. In contrast, the larger *NSR*  
600 in f3-H indicates that stronger stochastic forcing acts on a weaker ENSO signal, facilitating the irregular  
601 oscillation that more closely resembles the observation.

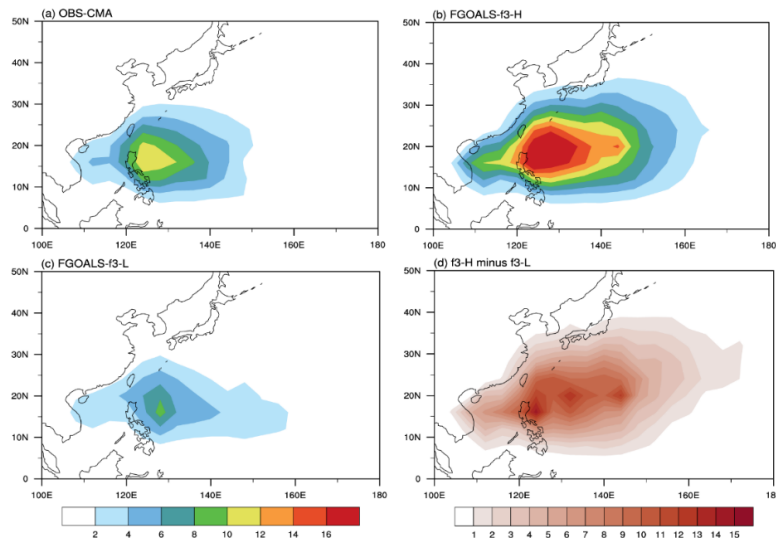
## 602 **5.2 Sources of differences in HF westerly wind activity: evaluation of TC and MJO**

603 To further explore the origin of difference in HF westerly wind intensity between f3-L and f3-H, we  
604 compare the simulated performance of TC and MJO activities in these two models. The results show that  
605 the differences in the HF westerly wind intensity are primarily related to the models' ability to reproduce  
606 TC activity. Figure 12 shows the spatial distribution of TCTD over the western North Pacific (WNP).  
607 The spatial distributions of TCTD in both f3-H and f3-L are similar to the observation, with TC tracks  
608 primarily located in the southwestern quadrant of WNP. Although both versions can reasonably  
609 reproduce the spatial distribution characteristics of TC activities over the WNP, a significant difference  
610 exists in TC frequency: TC activity is much more frequent in f3-H than that in f3-L. The difference map  
611 (Fig. 12d, f3-H minus f3-L) shows positive values almost everywhere north of the equator. It is worth  
612 noting that TCTD in f3-H remains relatively weak compared to the observation, which is a common  
613 simulation bias in most current climate models (Nakamura et al., 2017; Tang et al., 2022). Although f3-  
614 H still underestimates TC activity compared to the observation, this improvement relative to f3-L is  
615 substantial.



617 **Figure 12.** The averaged TC track density (TCTD, units: counts year<sup>-1</sup>) over western North Pacific for (a)  
 618 Observation (CMA), (b) f3-H, (c) f3-L and (d) the difference between f3-H and f3-L (f3-H minus f3-L).

619 Furthermore, we compare the difference in the TC intensity between f3-H and f3-L. Figure 13 shows  
 620 the spatial distribution of ACE index over WNP in the observation and the models. Both models show  
 621 that strong TC activity is primarily concentrated east of the Philippines sea, consistent with the  
 622 observation (Ma et al., 2025). However, the ACE index in f3-H is significantly stronger than that in f3-  
 623 L, indicating stronger TC activity in f3-H. In summary, the TC activity over WNP is more frequent and  
 624 intense in f3-H than that in f3-L, which largely explains the stronger HF westerly wind anomalies in f3-  
 625 H.

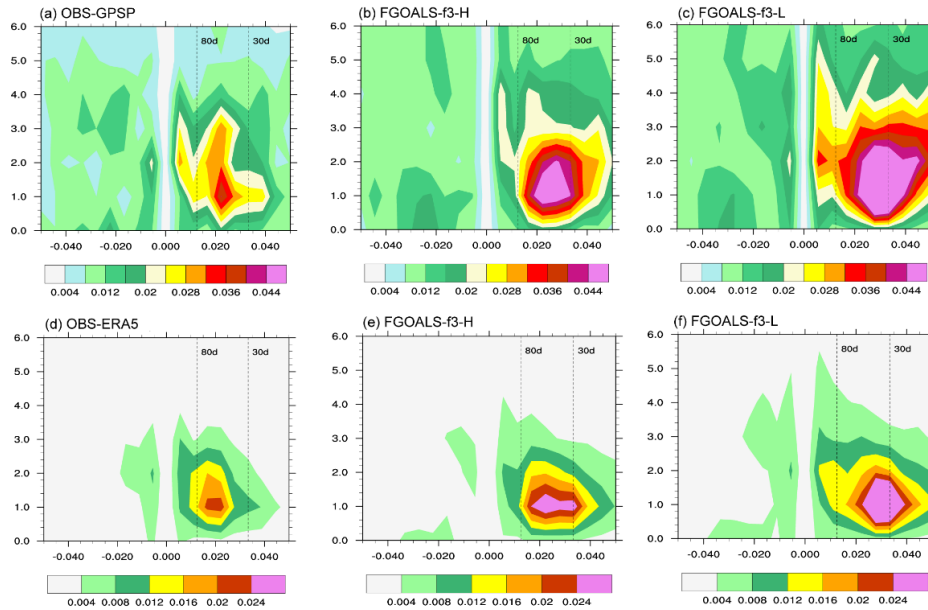


627 **Figure 13.** The averaged accumulated cyclone energy (ACE, units: 10<sup>4</sup> knots year<sup>-1</sup>) over western North Pacific for  
 628 (a) Observation (CMA), (b) f3-H, (c) f3-L and (d) the difference between f3-H and f3-L (f3-H minus f3-L).

629 Model horizontal resolution is a key factor in TC simulation (Tang et al., 2022). In general, climate  
630 models with coarse resolutions ( $\geq 100$  km) tend to only reproduce TC-like structures (Camargo et al.,  
631 2005; Camargo and Wing, 2016), with activity that is relatively weak and infrequent (Camargo, 2013;  
632 Nakamura et al., 2017). As resolution increases, models can simulate more frequent and more intense TC  
633 activity (Roberts et al., 2020a; Tang et al., 2022). In particular, when the horizontal resolution is increased  
634 to 25 km, the simulation of TC spatial structure and associated wind fields is significantly improved,  
635 yielding more realistic characteristics of TC activity (Davis et al., 2018; Roberts et al., 2020b). The  
636 analysis results of the FGOALS-f3 models (Figs. 11 and 12) are consistent with these previous findings.  
637 Compared to the f3-L model (with a horizontal resolution of 100 km), the f3-H model (with a horizontal  
638 resolution of 25 km) provides a more realistic simulation of TC frequency and produces stronger TC  
639 intensities. This difference in TC simulation associated with model resolution modulates the intensity of  
640 HF westerly wind activity and hence influences the regularity of ENSO cycle in the two models.

641 On the other hand, we also examine the other primary source of HF westerly wind activity—the MJO.  
642 Figure 14 shows the wavenumber-frequency spectra of the space-time filtered precipitation and surface  
643 zonal wind. It can be seen that the spectral peak of precipitation and surface zonal wind in both models  
644 are concentrated at 30-80-day period, consistent with the observation. This indicates that both models  
645 reproduce the observed MJO timescales reasonably well. In terms of intensity, although the MJO-related  
646 precipitation and zonal wind fields are somewhat exaggerated in both models compared to the  
647 observation, the difference between f3-L and f3-H is small, especially for MJO-related zonal winds.  
648 Therefore, the difference in HF westerly wind activity is likely not directly linked to MJO activity.

649 Although finer resolution may improve model performance in certain aspects, these preliminary  
650 results show no significant improvement in MJO simulation from 100 km to 25 km in the case of these  
651 two FGOALS-f3 models. On the one hand, this may be because MJO simulation is heavily constrained  
652 by the accurate representation of physical processes like convection parameterization, boundary layer  
653 processes, and air-sea coupling. Thus, increased resolution must be combined with optimized physics  
654 schemes to effectively improve MJO simulation (Jiang et al., 2020b). On the other hand, recent studies  
655 suggest that significant MJO improvement can be seen when resolution increases to the kilometer-scale—  
656 the "convection-permitting resolution" (Savarin and Chen, 2022).



658 **Figure 14.** Wavenumber-frequency spectra of space-time filtered (a)–(c) precipitation (units: mm/day) and (d)–(f)  
 659 surface zonal wind fields (m/s) during the boreal winter (November to next August) for observation (left column),  
 660 f3-H (middle column) and f3-L (right column).

661 In summary, we find that the high-resolution version can better simulate TC activity, with more  
 662 frequent and stronger TCs over the WNP than the lower-resolution version. This difference results in  
 663 stronger HF westerly wind activity in f3-H than that in f3-L. Given that HF westerly wind activity acts  
 664 as a stochastic forcing on ENSO, the relatively weaker HF atmospheric noise in f3-L has a limited  
 665 randomizing effect on its stronger ENSO signal. In other words, the weaker HF zonal wind activity in  
 666 f3-L cannot overcome its inherently stronger ENSO signal, leading to overly regular oscillation in f3-L.  
 667 In contrast, f3-H has a weaker intrinsic ENSO signal but stronger "noise". Therefore, the ENSO cycle in  
 668 f3-L appears much more regular than that in f3-H.

## 669 6. Conclusions and implications

### 670 6.1 Conclusions

671 This study provides a process-based evaluation of how horizontal resolution influences ENSO  
 672 simulation in the CAS FGOALS-f3 climate system model. The comparison between its low-resolution  
 673 (f3-L, ~100 km) and high-resolution (f3-H, ~25 km) configurations reveals systematic and resolution-  
 674 dependent differences in ENSO amplitude, period, oscillation irregularity, and underlying air-sea  
 675 coupling processes.

676 A key structural source of bias in f3-L is the overly confined meridional structure of ENSO-related

677 zonal wind stress anomalies, which strengthens the thermocline and zonal-advection feedbacks and leads  
678 to an exaggerated ENSO amplitude. The process-oriented diagnosis based on ENSO-related air-sea  
679 coupling processes demonstrates that these feedbacks can be directly attributed to resolution-sensitive  
680 meridional distribution of equatorial zonal wind stress anomalies, indicating that resolving the meridional  
681 structure of wind forcing is essential for realistic representation of ENSO amplitude.

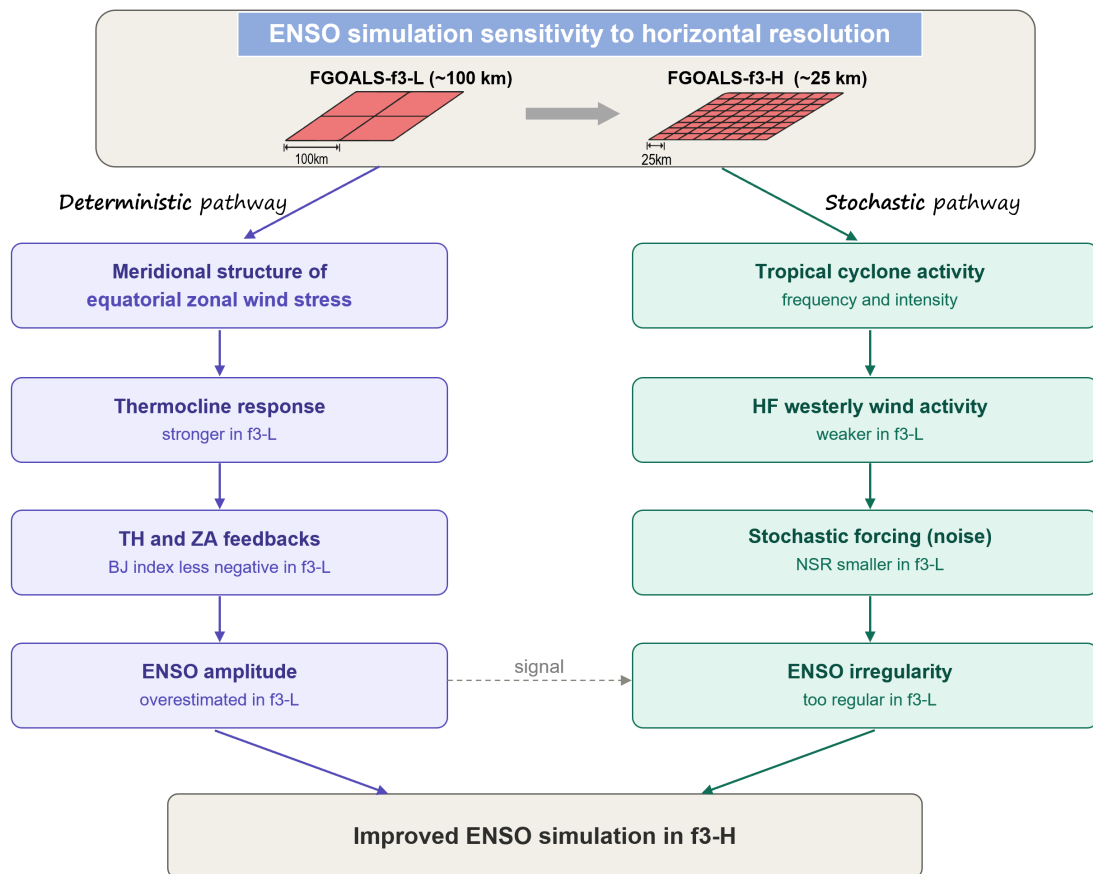
682 The excessive regularity of ENSO in f3-L is another resolution-driven bias, arising from insufficient  
683 HF atmospheric variability. The high-resolution configuration produces more realistic TC activity and  
684 more vigorous WWEs, which introduce stochastic forcing that disrupts the ENSO cycle and generates  
685 irregular variability closer to the observation. These results highlight that the representation of synoptic-  
686 scale atmospheric processes is integral to capturing observed temporal irregularity of ENSO.

687 Overall, this study demonstrates that ENSO-related biases in FGOALS-f3 arise from identifiable,  
688 resolution-sensitive structural features in the coupled system. Through two complementary diagnostic  
689 pathways, we provide a traceable and mechanistic explanation for how horizontal resolution modulates  
690 ENSO simulation (Figure 15). The diagnostic framework developed here is model-agnostic and  
691 reproducible, offering a practical tool for evaluating ENSO performance in other climate models and  
692 guiding future development of the FGOALS-f3 model family.

## 693 **6.2 Implications**

694 The findings from this study yield several actionable insights for FGOALS-f3 development and for  
695 the broader CMIP-class modeling community. (1) Improving the atmospheric representation of  
696 equatorial wind stress meridional gradient should be a development priority. (2) As shown in Figure 15,  
697 increase in horizontal resolution has impacts on ENSO dynamics from both deterministic and stochastic  
698 pathways: the deterministic aspect influencing ENSO behaviors is via air-sea coupling processes, and  
699 the stochastic aspect influencing ENSO behaviors is via HF wind activity, both of which should be  
700 explicitly considered in future model evaluation framework. (3) The diagnostics applied here are model-  
701 agnostic and can serve as a reproducible framework for assessing resolution effects in other climate  
702 models participating in CMIP6/CMIP7. We encourage the community to adopt the process-oriented  
703 diagnostics presented here as a complement to conventional statistical metrics, so that the improvements  
704 in ENSO simulation can be traced back to specific physical mechanisms rather than assessed solely by  
705 outcome-based indices. (4) The ~25 km atmosphere resolution of f3-H improves both the air-sea coupling

706 processes and the stochastic forcing mechanisms, supporting the ongoing efforts toward next-generation  
 707 high-resolution climate models. However, the computational cost increases substantially from f3-L to f3-  
 708 H. The low-resolution version runs on 384 processor cores and achieves a throughput of approximately  
 709 15–20 model years per wall-clock day, whereas the high-resolution version requires 6,144 processor  
 710 cores and achieves only ~0.25 model years per wall-clock day. This sharp increase in computational  
 711 expense makes century-scale ensemble simulations with high-resolution models, such as f3-H,  
 712 considerably more demanding. Such a cost–benefit trade-off further motivates the development of  
 713 variable-resolution modeling frameworks (e.g., the Model for Prediction Across Scales and the  
 714 ICOSahedral Nonhydrostatic model), which can selectively refine the grid over the tropical Pacific to  
 715 capture these resolution-sensitive processes while maintaining coarser resolution elsewhere.



717 **Figure 15.** Schematic diagram illustrating how increased horizontal resolution (~100 km to ~25 km) improves ENSO  
 718 simulation in FGOALS-f3 via both the deterministic feedback processes and the stochastic atmospheric forcing  
 719 pathways.

720

721

722 *Data and Code availability.* Source codes of the FGOALS-f3 model used in this study and the analysis  
723 scripts are archived at <https://doi.org/10.5281/zenodo.19552337> (Song et al., 2026). The model output of  
724 FGOALS-f3 models described in this paper is distributed through the Earth System Grid Federation  
725 (ESGF) and is freely obtained via the ESGF data portals after registration (<https://aims2.llnl.gov/search>,  
726 last access: 27 November 2025). All the observation and reanalysis datasets are available online and  
727 publicly available as cited in the references. The ORAS5 and ERA-5 datasets are obtained from  
728 <https://cds.climate.copernicus.eu/datasets>. The HadISST dataset is from  
729 <https://www.metoffice.gov.uk/hadobs/hadisst/data/download.html>. The GPCP dataset is available at  
730 <https://www.ncei.noaa.gov/data/global-precipitation-climatology-project-gpcp-daily/access>. The  
731 SODA2.2.4 dataset can be accessed at [http://apdrc.soest.hawaii.edu/datadoc/soda\\_2.2.4.php](http://apdrc.soest.hawaii.edu/datadoc/soda_2.2.4.php). The CMA  
732 TC best track dataset is from <https://tcdata.typhoon.org.cn/en/zjljsjj.html>. The description and data for  
733 HighResSST-present simulations of FGOALS-f3 can be found at  
734 <https://doi.org/10.22033/ESGF/CMIP6.3312> (Bao and He, 2019; Bao et al., 2020).

735 *Author contribution.* All authors contributed to the study conception and design. Material preparation,  
736 data collection and analysis were performed by MS and LC. JZ contributed to the application of methods  
737 related to TC detection. The first draft of the manuscript was written by MS and LC. QY, BA and HZ  
738 discussed the results and commented on the manuscript. All authors read and approved the final  
739 manuscript.

740 *Competing interests.* The authors declare that they have no conflict of interest.

741 *Disclaimer.* Publisher's note: Copernicus Publications remains neutral with regard to jurisdictional  
742 claims made in the text, published maps, institutional affiliations, or any other geographical  
743 representation in this paper. While Copernicus Publications makes every effort to include appropriate  
744 place names, the final responsibility lies with the authors. Views expressed in the text are those of the  
745 authors and do not necessarily reflect the views of the publisher.

746 *Acknowledgements.* We acknowledge the High Performance Computing Center of Nanjing University of  
747 Information Science & Technology for their support of this work.

748 *Financial support.* This work was the jointly supported by the National Key Research and Development  
749 Program of China (Grant 2022YFF0802004), NSFC (No. 42576024), the Excellent Youth Natural

750 Science Foundation of Jiangsu Province (BK20230061) and Postgraduate Research & Practice  
751 Innovation Program of Jiangsu Province (KYCX24\_1417).

752

753 **Reference**

754 Adler, R. F., Huffman, G. J., Chang, A., Ferraro, R., Xie, P.-P., Janowiak, J., Rudolf, B., Schneider, U.,  
755 Curtis, S., Bolvin, D., Gruber, A., Susskind, J., Arkin, P., and Nelkin, E.: The version-2 global  
756 precipitation climatology project (GPCP) monthly precipitation analysis (1979–present), *Journal of*  
757 *Hydrometeorology*, 4, 1147–1167, [https://doi.org/10.1175/1525-](https://doi.org/10.1175/1525-7541(2003)004%3C1147:TVGPCP%3E2.0.CO;2)  
758 [7541\(2003\)004%3C1147:TVGPCP%3E2.0.CO;2](https://doi.org/10.1175/1525-7541(2003)004%3C1147:TVGPCP%3E2.0.CO;2), 2003.

759 An, B., Yu, Y. Q., Bao, Q., He, B., Li, J. X., Luan, Y. H., Chen, K. J., and Zheng, W. P.: CAS FGOALS-  
760 f3-H dataset for the high-resolution model intercomparison project (HighResMIP) Tier 2, *Advances*  
761 *in Atmospheric Sciences*, 39, 1873–1884, <https://doi.org/10.1007/s00376-022-2030-5>, 2022.

762 Bacmeister, J. T., Wehner, M. F., Neale, R. B., Gettelman, A., Hannay, C., Lauritzen, P. H., Caron, J. M.,  
763 and Truesdale, J. E.: Exploratory high-resolution climate simulations using the community  
764 atmosphere model (CAM), *Journal of Climate*, 27, 3073–3099, [https://doi.org/10.1175/jcli-d-13-](https://doi.org/10.1175/jcli-d-13-00387.1)  
765 [00387.1](https://doi.org/10.1175/jcli-d-13-00387.1), 2014.

766 Bao, Q., Liu, Y. M., Wu, G. X., He, B., Li, J. X., Wang, L., Wu, X. F., Chen, K. J., Wang, X. C., Yang, J.,  
767 and Zhang, X. Q.: CAS FGOALS-f3-H and CAS FGOALS-f3-L outputs for the high-resolution  
768 model intercomparison project simulation of CMIP6, *Atmospheric and Oceanic Science Letters*, 13,  
769 576–581, <https://doi.org/10.1080/16742834.2020.1814675>, 2020.

770 Bao, Q. and He, B.: CAS FGOALS-f3-H model output prepared for CMIP6 HighResMIP highresSST-  
771 present, Earth System Grid Federation [data set], <https://doi.org/10.22033/ESGF/CMIP6.3312>,  
772 2019

773 Barnston, A. G., Tippett, M. K., L'Heureux, M. L., Li, S., and DeWitt, D. G.: Skill of real-time seasonal  
774 ENSO model predictions during 2002–11: Is our capability increasing?, *Bulletin of the American*  
775 *Meteorological Society*, 93, 631–651, <https://doi.org/10.1175/bams-d-11-00111.1>, 2012.

776 Bell, G. D., Halpert, M. S., Schnell, R. C., Higgins, R. W., Lawrimore, J., Kousky, V. E., Tinker, R.,  
777 Thiaw, W., Chelliah, M., and Artusa, A.: Climate assessment for 1999, *Bulletin of the American*

778 Meteorological Society, 81, s1–s50, [https://doi.org/10.1175/1520-0477\(2000\)81\[s1:CAF\]2.0.CO;2](https://doi.org/10.1175/1520-0477(2000)81[s1:CAF]2.0.CO;2),  
779 2000.

780 Cai, W. J., Santoso, A., Collins, M., Dewitte, B., Karamperidou, C., Kug, J.-S., Lengaigne, M., McPhaden,  
781 M. J., Stuecker, M. F., Taschetto, A. S., Timmermann, A., Wu, L. X., Yeh, S.-W., Wang, G., Ng, B.,  
782 Jia, F., Yang, Y., Ying, J., Zheng, X.-T., Bayr, T., Brown, J. R., Capotondi, A., Cobb, K. M., Gan, B.,  
783 Geng, T., Ham, Y.-G., Jin, F.-F., Jo, H.-S., Li, X., Lin, X., McGregor, S., Park, J.-H., Stein, K., Yang,  
784 K., Zhang, L., and Zhong, W. X.: Changing El Niño–Southern Oscillation in a warming climate,  
785 *Nature Reviews Earth and Environment*, 2, 628–644, <https://doi.org/10.1038/s43017-021-00199-z>,  
786 2021.

787 Camargo, S. J., Barnston, A. G., and Zebiak, S. E.: A statistical assessment of tropical cyclone activity in  
788 atmospheric general circulation models, *Tellus A: Dynamic Meteorology and Oceanography*, 57,  
789 589–604, <https://doi.org/10.3402/tellusa.v57i4.14705>, 2005.

790 Camargo, S. J.: Global and regional aspects of tropical cyclone activity in the CMIP5 models, *Journal of*  
791 *Climate*, 26, 9880–9902, <https://doi.org/10.1175/jcli-d-12-00549.1>, 2013.

792 Camargo, S. J. and Wing, A. A.: Tropical cyclones in climate models, *Wiley Interdisciplinary Reviews:*  
793 *Climate Change*, 7, 211–237, <https://doi.org/10.1002/wcc.373>, 2016.

794 Carton, J. A. and Giese, B. S.: A Reanalysis of Ocean Climate Using Simple Ocean Data Assimilation  
795 (SODA), *Monthly Weather Review*, 136, 2999–3017, <https://doi.org/10.1175/2007mwr1978.1>,  
796 2008.

797 Chang, P., Zhang, S. Q., Danabasoglu, G., Yeager, S. G., Fu, H. H., Wang, H., Castruccio, F. S., Chen,  
798 Y., Edwards, J., Fu, D., Jia, Y., Laurindo, L. C., Liu, X., Rosenbloom, N., Small, R. J., Xu, G. P.,  
799 Zeng, Y. H., Zhang, Q. Y., Bacmeister, J., Bailey, D. A., Duan, X., DuVivier, A. K., Li, D. P., Li, Y.  
800 X., Neale, R., Stössel, A., Wang, L., Zhuang, Y., Baker, A., Bates, S., Dennis, J., Diao, X., Gan, B.  
801 L., Gopal, A., Jia, D. N., Jing, Z., Ma, X., Saravanan, R., Strand, W. G., Tao, J., Yang, H. Y., Wang,  
802 X. Q., Wei, Z. Q., and Wu, L. X.: An unprecedented set of high-resolution earth system simulations  
803 for understanding multiscale interactions in climate variability and change, *Journal of Advances in*  
804 *Modeling Earth Systems*, 12, e2020MS002298, <https://doi.org/10.1029/2020ms002298>, 2020.

805 Chen, D. K., Lian, T., Fu, C., Cane, M. A., Tang, Y. M., Murtugudde, R., Song, X. S., Wu, Q. Y., and  
806 Zhou, L.: Strong influence of westerly wind bursts on El Niño diversity, *Nature Geoscience*, 8, 339–

807 345, <https://doi.org/10.1038/ngeo2399>, 2015a.

808 Chen, L., Li, T., and Yu, Y. Q.: Causes of strengthening and weakening of ENSO amplitude under global  
809 warming in four CMIP5 models, *Journal of Climate*, 28, 3250–3274, [https://doi.org/10.1175/jcli-d-](https://doi.org/10.1175/jcli-d-14-00439.1)  
810 14-00439.1, 2015b.

811 Chen, L., Yu, Y. Q., and Zheng, W. P.: Improved ENSO simulation from climate system model FGOALS-  
812 g1.0 to FGOALS-g2, *Climate Dynamics*, 47, 2617–2634, [https://doi.org/10.1007/s00382-016-](https://doi.org/10.1007/s00382-016-2988-8)  
813 2988-8, 2016a.

814 Chen, L., Li, T., Behera, S. K., and Doi, T.: Distinctive precursory air–sea signals between regular and  
815 super El Niños, *Advances in Atmospheric Sciences*, 33, 996–1004, [https://doi.org/10.1007/s00376-](https://doi.org/10.1007/s00376-016-5250-8)  
816 016-5250-8, 2016b.

817 Chen, L., Li, T., Wang, B., and Wang, L.: Formation mechanism for 2015/16 super El Nino, *Scientific*  
818 *Reports*, 7, 2975–2985, <https://doi.org/10.1038/s41598-017-02926-3>, 2017.

819 Chen, L., Wang, L., Li, T., and Liu, J.: Drivers of reduced ENSO variability in mid-Holocene in a coupled  
820 model, *Climate Dynamics*, 52, 5999–6014, <https://doi.org/10.1007/s00382-018-4496-5>, 2019a.

821 Chen, L., Zheng, W., and Braconnot, P.: Towards understanding the suppressed ENSO activity during  
822 mid-Holocene in PMIP2 and PMIP3 simulations, *Climate Dynamics*, 53, 1095–1110,  
823 <https://doi.org/10.1007/s00382-019-04637-z>, 2019b.

824 Craig, A. P., Vertenstein, M., and Jacob, R.: A new flexible coupler for earth system modeling developed  
825 for CCSM4 and CESM1, *The International Journal of High Performance Computing Applications*,  
826 26, 31–42, <https://doi.org/10.1177/1094342011428141>, 2012.

827 Davis, C. A.: Resolving tropical cyclone intensity in models, *Geophysical Research Letters*, 45, 2082–  
828 2087, <https://doi.org/10.1002/2017GL076966>, 2018.

829 Dawson, A., Matthews, A. J., Stevens, D. P., Roberts, M. J., and Vidale, P. L.: Importance of oceanic  
830 resolution and mean state on the extra-tropical response to El Niño in a matrix of coupled models,  
831 *Climate Dynamics*, 41, 1439–1452, <https://doi.org/10.1007/s00382-012-1518-6>, 2013.

832 Docquier, D., Grist, J. P., Roberts, M. J., Roberts, C. D., Semmler, T., Ponsoni, L., Massonnet, F.,  
833 Sidorenko, D., Sein, D. V., Iovino, D., Bellucci, A., and Fichet, T.: Impact of model resolution on  
834 Arctic sea ice and North Atlantic Ocean heat transport, *Climate Dynamics*, 53, 4989–5017,  
835 <https://doi.org/10.1007/s00382-019-04840-y>, 2019.

836 Eisenman, I., Yu, L. S., and Tziperman, E.: Westerly wind bursts: ENSO's tail rather than the dog?,  
837 *Journal of Climate*, 18, 5224–5237, <https://doi.org/10.1175/JCLI3588.1>, 2005.

838 Eyring, V., Bony, S., Meehl, G. A., Senior, C. A., Stevens, B., Stouffer, R. J., and Taylor, K. E.: Overview  
839 of the Coupled Model Intercomparison Project Phase 6 (CMIP6) experimental design and  
840 organization, *Geoscientific Model Development*, 9, 1937–1958, [https://doi.org/10.5194/gmd-9-](https://doi.org/10.5194/gmd-9-1937-2016)  
841 [1937-2016](https://doi.org/10.5194/gmd-9-1937-2016), 2016.

842 Fedorov, A. V.: The response of the coupled tropical ocean–atmosphere to westerly wind bursts,  
843 *Quarterly Journal of the Royal Meteorological Society*, 128, 1–23,  
844 <https://doi.org/10.1002/qj.200212857901>, 2002.

845 Fedorov, A. V., Hu, S. N., Lengaigne, M., and Guilyardi, E.: The impact of westerly wind bursts and  
846 ocean initial state on the development, and diversity of El Niño events, *Climate Dynamics*, 44,  
847 1381–1401, <https://doi.org/10.1007/s00382-014-2126-4>, 2015.

848 Gebbie, G., Eisenman, I., Wittenberg, A., and Tziperman, E.: Modulation of westerly wind bursts by sea  
849 surface temperature: A semistochastic feedback for ENSO, *Journal of the Atmospheric Sciences*, 64,  
850 3281–3295, <https://doi.org/10.1175/jas4029.1>, 2007.

851 Gebbie, G. and Tziperman, E.: Incorporating a semi-stochastic model of ocean-modulated westerly wind  
852 bursts into an ENSO prediction model, *Theoretical and Applied Climatology*, 97, 65–73,  
853 <https://doi.org/10.1007/s00704-008-0069-6>, 2009.

854 Griffies, S. M., Danabasoglu, G., Durack, P. J., Adcroft, A. J., Balaji, V., Böning, C. W., Chassignet, E.  
855 P., Curchitser, E., Deshayes, J., Drange, H., Fox-Kemper, B., Gleckler, P. J., Gregory, J. M., Haak,  
856 H., Hallberg, R. W., Heimbach, P., Hewitt, H. T., Holland, D. M., Ilyina, T., Jungclaus, J. H., Komuro,  
857 Y., Krasting, J. P., Large, W. G., Marsland, S. J., Masina, S., McDougall, T. J., Nurser, A. J. G., Orr,  
858 J. C., Pirani, A., Qiao, F. I., Stouffer, R. J., Taylor, K. E., Treguier, A. M., Tsujino, H., Uotila, P.,  
859 Valdivieso, M., Wang, Q., Winton, M., and Yeager, S. G.: OMIP contribution to CMIP6:  
860 experimental and diagnostic protocol for the physical component of the Ocean Model  
861 Intercomparison Project, *Geoscientific Model Development*, 9, 3231–3296,  
862 <https://doi.org/10.5194/gmd-9-3231-2016>, 2016.

863 Guilyardi, E., Gualdi, S., Slingo, J., Navarra, A., Delecluse, P., Cole, J., Madec, G., Roberts, M., Latif,  
864 M., and Terray, L.: Representing El Niño in coupled ocean–atmosphere GCMs: The dominant role

865 of the atmospheric component, *Journal of Climate*, 17, 4623–4629, <https://doi.org/10.1175/JCLI->  
866 3260.1, 2004.

867 Guilyardi, E., Capotondi, A., Lengaigne, M., Thual, S., and Wittenberg, A. T.: ENSO modeling: History,  
868 progress, and challenges, in: *El Niño Southern Oscillation in a Changing Climate*, edited by:  
869 McPhaden, M. J., Santoso, A., and Cai, W., American Geophysical Union, American, 199-226,  
870 <https://doi.org/10.1002/9781119548164.ch9>, 2020.

871 Hallberg, R.: Using a resolution function to regulate parameterizations of oceanic mesoscale eddy effects,  
872 *Ocean Modelling*, 72, 92–103, <https://doi.org/10.1016/j.ocemod.2013.08.007>, 2013.

873 Harrison, D. E. and Vecchi, G. A.: Westerly wind events in the tropical Pacific, 1986–95\*, *Journal of*  
874 *Climate*, 10, 3131–3156, [https://doi.org/10.1175/1520-0442\(1997\)010<3131:Wweitt>2.0.Co;2](https://doi.org/10.1175/1520-0442(1997)010<3131:Wweitt>2.0.Co;2),  
875 1997.

876 He, B., Bao, Q., Wang, X. C., Zhou, L. J., Wu, X. F., Liu, Y. M., Wu, G. X., Chen, K. J., He, S. C., Hu,  
877 W. T., Li, J. D., Li, J. X., Nian, G. K., Wang, L., Yang, J., Zhang, M. H., and Zhang, X. Q.: CAS  
878 FGOALS-f3-L model datasets for CMIP6 historical atmospheric model intercomparison project  
879 simulation, *Advances in Atmospheric Sciences*, 36, 771–778, <https://doi.org/10.1007/s00376-019->  
880 9027-8, 2019.

881 He, B., He, X. Y., Liu, Y. M., Wu, G. X., Bao, Q., Hu, W. T., Sheng, C., and Feng, S. J.: Role of thermal  
882 and dynamical subdaily perturbations over the Tibetan Plateau in 30-day extended-range forecast  
883 of East Asian precipitation in early summer, *npj Climate and Atmospheric Science*, 8,  
884 <https://doi.org/10.1038/s41612-025-00931-2>, 2025a.

885 He, X.-Y., He, B., Bao, Q., Liu, Y.-M., Li, J.-D., Wang, X.-C., Chen, X.-C., and Wu, G.-X.: The sensitivity  
886 of the Asian summer monsoon simulation to horizontal resolution and air–sea coupling in the  
887 FGOALS-f climate system model, *Advances in Climate Change Research*, 16, 44 – 57,  
888 <https://doi.org/10.1016/j.accre.2025.01.008>, 2025b.

889 Hersbach, H., Bell, B., Berrisford, P., Hirahara, S., Horányi, A., Muñoz-Sabater, J., Nicolas, J., Peubey,  
890 C., Radu, R., Schepers, D., Simmons, A., Soci, C., Abdalla, S., Abellan, X., Balsamo, G., Bechtold,  
891 P., Biavati, G., Bidlot, J., Bonavita, M., De Chiara, G., Dahlgren, P., Dee, D., Diamantakis, M.,  
892 Dragani, R., Flemming, J., Forbes, R., Fuentes, M., Geer, A., Haimberger, L., Healy, S., Hogan, R.  
893 J., Hólm, E., Janisková, M., Keeley, S., Laloyaux, P., Lopez, P., Lupu, C., Radnoti, G., de Rosnay,

894 P., Rozum, I., Vamborg, F., Villaume, S., and Thépaut, J. N.: The ERA5 global reanalysis, *Quarterly*  
895 *Journal of the Royal Meteorological Society*, 146, 1999–2049, <https://doi.org/10.1002/qj.3803>,  
896 2020.

897 Hewitt, H. T., Roberts, M. J., Hyder, P., Graham, T., Rae, J., Belcher, S. E., Bourdallé-Badie, R., Copsey,  
898 D., Coward, A., Guiavarch, C., Harris, C., Hill, R., Hirschi, J. J. M., Madec, G., Mizielinski, M. S.,  
899 Neininger, E., New, A. L., Rioual, J.-C., Sinha, B., Storkey, D., Shelly, A., Thorpe, L., and Wood,  
900 R. A.: The impact of resolving the Rossby radius at mid-latitudes in the ocean: results from a high-  
901 resolution version of the Met Office GC2 coupled model, *Geoscientific Model Development*, 9,  
902 3655–3670, <https://doi.org/10.5194/gmd-9-3655-2016>, 2016.

903 Hua, L. J., Chen, L., Rong, X. Y., Su, J. Z., Wang, L., Li, T., and Yu, Y. Q.: Impact of atmospheric model  
904 resolution on simulation of ENSO feedback processes: a coupled model study, *Climate Dynamics*,  
905 51, 3077–3092, <https://doi.org/10.1007/s00382-017-4066-2>, 2018.

906 Hunke, E. C. and Lipscomb, W. H.: CICE: The Los Alamos Sea Ice Model, Documentation and Software  
907 User’s Manual, Version 4.1, Tech. Rep. LA-CC-06-012, Los Alamos National Laboratory, Los  
908 Alamos, New Mexico, available at: <http://oceans11.lanl.gov/trac/CICE>, 2010.

909 Jiang, W. P., Huang, P., Li, G., and Huang, G.: Emergent constraint on the frequency of central Pacific  
910 El Niño under global warming by the equatorial Pacific cold tongue bias in CMIP5/6 models,  
911 *Geophysical Research Letters*, 47, <https://doi.org/10.1029/2020gl089519>, 2020a.

912 Jiang, W. P., Huang, P., Huang, G., and Ying, J.: Origins of the excessive westward extension of ENSO  
913 SST simulated in CMIP5 and CMIP6 models, *Journal of Climate*, 34, 2839–2851,  
914 <https://doi.org/10.1175/jcli-d-20-0551.1>, 2021.

915 Jiang, X. N., Adames, Á. F., Kim, D., Maloney, E. D., Lin, H., Kim, H., Zhang, C. D., DeMott, C. A.,  
916 and Klingaman, N. P.: Fifty years of research on the Madden-Julian Oscillation: Recent progress,  
917 challenges, and perspectives, *Journal of Geophysical Research: Atmospheres*, 125,  
918 <https://doi.org/10.1029/2019jd030911>, 2020b.

919 Jin, F.-F.: An equatorial ocean recharge paradigm for ENSO. Part I: Conceptual model, *Journal of the*  
920 *Atmospheric Sciences*, 54, 811–829, [https://doi.org/10.1175/1520-](https://doi.org/10.1175/1520-0469(1997)054<0811:Aeorpf>2.0.Co;2)  
921 [0469\(1997\)054<0811:Aeorpf>2.0.Co;2](https://doi.org/10.1175/1520-0469(1997)054<0811:Aeorpf>2.0.Co;2), 1997.

922 Jin, F. F., Kim, S. T., and Bejarano, L.: A coupled-stability index for ENSO, *Geophysical Research Letters*,

923 33, <https://doi.org/10.1029/2006gl027221>, 2006.

924 Kim, S. T. and Jin, F.-F.: An ENSO stability analysis. Part II: Results from the twentieth and twenty-first  
925 century simulations of the CMIP3 models, *Climate Dynamics*, 36, 1609–1627,  
926 <https://doi.org/10.1007/s00382-010-0872-5>, 2011a.

927 Kim, S. T. and Jin, F.-F.: An ENSO stability analysis. Part I: results from a hybrid coupled model, *Climate*  
928 *Dynamics*, 36, 1593–1607, <https://doi.org/10.1007/s00382-010-0796-0>, 2011b.

929 Kreussler, P., Caron, L. P., Wild, S., Loosveldt Tomas, S., Chauvin, F., Moine, M. P., Roberts, M. J.,  
930 Ruprich-Robert, Y., Seddon, J., Valcke, S., Vannière, B., and Vidale, P. L.: Tropical cyclone  
931 integrated kinetic energy in an ensemble of HighResMIP simulations, *Geophysical Research Letters*,  
932 48, <https://doi.org/10.1029/2020gl090963>, 2021.

933 Lawrence, D. M., Oleson, K. W., Flanner, M. G., Thornton, P. E., Swenson, S. C., Lawrence, P. J., Zeng,  
934 X., Yang, Z. L., Levis, S., and Sakaguchi, K.: Parameterization improvements and functional and  
935 structural advances in version 4 of the Community Land Model, *Journal of Advances in Modeling*  
936 *Earth Systems*, 3, <https://doi.org/10.1029/2011MS00045>, 2011.

937 Li, J., Yu, Y. Q., and Sun, D. Z.: Asymmetric Responses in the Equatorial Pacific to Wind Forcing in  
938 OMIP2 Experiments: Role of Zonal Currents, *Geophysical Research Letters*, 52, e2025GL114661,  
939 <https://doi.org/10.1029/2025gl114661>, 2025.

940 Li, J. X., Bao, Q., Liu, Y. M., Wang, L., Yang, J., Wu, G. X., Wu, X. F., He, B., Wang, X. C., Zhang, X.  
941 Q., Yang, Y. X., and Shen, Z. L.: Effect of horizontal resolution on the simulation of tropical  
942 cyclones in the Chinese Academy of Sciences FGOALS-f3 climate system model, *Geoscientific*  
943 *Model Development*, 14, 6113–6133, <https://doi.org/10.5194/gmd-14-6113-2021>, 2021.

944 Li, T.: Phase transition of the El Niño–Southern Oscillation: A stationary SST mode, *Journal of the*  
945 *atmospheric sciences*, 54, 2872–2887, [https://doi.org/10.1175/1520-0469\(1997\)054<2872:PTOTEN>2.0.CO;2](https://doi.org/10.1175/1520-0469(1997)054<2872:PTOTEN>2.0.CO;2), 1997.

947 Li, T. Y., Yu, Y. Q., An, B., Luan, Y. H., and Chen, K. J.: Tropical instability waves in a high-resolution  
948 oceanic and coupled GCM, *Ocean Modelling*, 182, <https://doi.org/10.1016/j.ocemod.2023.102169>,  
949 2023.

950 Li, Y., Liu, H., Ding, M., Lin, P., Yu, Z., Yu, Y., Meng, Y., Li, Y., Jian, X., and Jiang, J.: Eddy-resolving  
951 simulation of CAS-LICOM3 for phase 2 of the ocean model intercomparison project, *Advances in*

952 Atmospheric Sciences, 37, 1067–1080, <https://doi.org/10.1007/s00376-020-0057-z>, 2020.

953 Liang, Y. and Fedorov, A. V.: Linking the Madden–Julian Oscillation, tropical cyclones and westerly  
954 wind bursts as part of El Niño development, *Climate Dynamics*, 57, 1039–1060,  
955 <https://doi.org/10.1007/s00382-021-05757-1>, 2021.

956 Liao, H. X., Cai, Z. C., Guo, J. S., and Song, Z. Y.: Effects of ITCZ poleward location bias on ENSO  
957 seasonal phase-locking simulation in climate models, *Journal of Climate*, 36, 5233–5249,  
958 <https://doi.org/10.1175/jcli-d-22-0891.1>, 2023.

959 Lu, B., Jin, F.-F., and Ren, H.-L.: A coupled dynamic index for ENSO periodicity, *Journal of Climate*,  
960 31, 2361–2376, <https://doi.org/10.1175/jcli-d-17-0466.1>, 2018.

961 Lu, X. Q., Yu, H., Ying, M., Zhao, B. K., Zhang, S., Lin, L. M., Bai, L. N., and Wan, R. J.: Western north  
962 Pacific tropical cyclone database created by the China Meteorological Administration, *Advances in*  
963 *Atmospheric Sciences*, 38, 690–699, <https://doi.org/https://10.1007/s00376-020-0211-7>, 2021.

964 Ma, T., Yu, W.-D., Speich, S., Zhao, H.-K., Xin, R., Luo, H., and Wu, L.-G.: Philippine archipelago and  
965 South China Sea monsoon plus ocean cooling buffer Northwestern Pacific super typhoons, *Nature*  
966 *Communications*, 16, <https://doi.org/10.1038/s41467-025-62334-4>, 2025.

967 Madden, R. A. and Julian, P. R.: Detection of a 40–50 day oscillation in the zonal wind in the tropical  
968 Pacific, *Journal of Atmospheric Sciences*, 28, 702–708, [https://doi.org/10.1175/1520-0469\(1971\)028%3C0702:DOADOI%3E2.0.CO;2](https://doi.org/10.1175/1520-0469(1971)028%3C0702:DOADOI%3E2.0.CO;2), 1971.

970 Madden, R. A. and Julian, P. R.: Description of global-scale circulation cells in the tropics with a 40–50  
971 day period, *Journal of Atmospheric Sciences*, 29, 1109–1123, [https://doi.org/10.1175/1520-0469\(1972\)029%3C1109:DOGSCC%3E2.0.CO;2](https://doi.org/10.1175/1520-0469(1972)029%3C1109:DOGSCC%3E2.0.CO;2), 1972.

973 McPhaden, M. J., Zebiak, S. E., and Glantz, M. H.: ENSO as an integrating concept in earth science,  
974 *Science*, 314, 1740–1745, <https://doi.org/10.1126/science.1132588>, 2006.

975 Moore, A. M. and Kleeman, R.: Stochastic forcing of ENSO by the intraseasonal oscillation, *Journal of*  
976 *Climate*, 12, 1199–1220, [https://doi.org/10.1175/1520-0442\(1999\)012<1199:Sfoebt>2.0.Co;2](https://doi.org/10.1175/1520-0442(1999)012<1199:Sfoebt>2.0.Co;2),  
977 1999.

978 Nakamura, J., Camargo, S. J., Sobel, A. H., Henderson, N., Emanuel, K. A., Kumar, A., LaRow, T. E.,  
979 Murakami, H., Roberts, M. J., Scoccimarro, E., Vidale, P. L., Wang, H., Wehner, M. F., and Zhao,  
980 M.: Western North Pacific Tropical Cyclone Model Tracks in Present and Future Climates, *Journal*

981 of Geophysical Research: Atmospheres, 122, 9721–9744, <https://doi.org/10.1002/2017jd027007>,  
982 2017.

983 Navarra, A., Gualdi, S., Masina, S., Behera, S., Luo, J. J., Masson, S., Guilyardi, E., Delecluse, P., and  
984 Yamagata, T.: Atmospheric horizontal resolution affects tropical climate variability in coupled  
985 models, *Journal of Climate*, 21, 730–750, <https://doi.org/10.1175/2007jcli1406.1>, 2008.

986 Planton, Y. Y., Guilyardi, E., Wittenberg, A. T., Lee, J., Gleckler, P. J., Bayr, T., McGregor, S., McPhaden,  
987 M. J., Power, S., Roehrig, R., Vialard, J., and Voltaire, A.: Evaluating climate models with the  
988 CLIVAR 2020 ENSO metrics package, *Bulletin of the American Meteorological Society*, 102,  
989 E193–E217, <https://doi.org/10.1175/bams-d-19-0337.1>, 2021.

990 Rayner, N. A., Parker, D. E., Horton, E. B., Folland, C. K., Alexander, L. V., Rowell, D. P., Kent, E. C.,  
991 and Kaplan, A.: Global analyses of sea surface temperature, sea ice, and night marine air  
992 temperature since the late nineteenth century, *Journal of Geophysical Research: Atmospheres*, 108,  
993 <https://doi.org/10.1029/2002jd002670>, 2003.

994 Roberts, M. J., Camp, J., Seddon, J., Vidale, P. L., Hodges, K., Vanniere, B., Mecking, J., Haarsma, R.,  
995 Bellucci, A., Scoccimarro, E., Caron, L.-P., Chauvin, F., Terray, L., Valcke, S., Moine, M.-P.,  
996 Putrasahan, D., Roberts, C., Senan, R., Zarzycki, C., and Ullrich, P.: Impact of model resolution on  
997 tropical cyclone simulation using the HighResMIP–PRIMAVERA multimodel ensemble, *Journal*  
998 *of Climate*, 33, 2557–2583, <https://doi.org/10.1175/jcli-d-19-0639.1>, 2020a.

999 Roberts, M. J., Camp, J., Seddon, J., Vidale, P. L., Hodges, K., Vannière, B., Mecking, J., Haarsma, R.,  
1000 Bellucci, A., Scoccimarro, E., Caron, L. P., Chauvin, F., Terray, L., Valcke, S., Moine, M. P.,  
1001 Putrasahan, D., Roberts, C. D., Senan, R., Zarzycki, C., Ullrich, P., Yamada, Y., Mizuta, R., Kodama,  
1002 C., Fu, D., Zhang, Q., Danabasoglu, G., Rosenbloom, N., Wang, H., and Wu, L.: Projected future  
1003 changes in tropical cyclones using the CMIP6 HighResMIP multimodel ensemble, *Geophysical*  
1004 *Research Letters*, 47, e2020GL088662, <https://doi.org/10.1029/2020gl088662>, 2020b.

1005 Roberts, M. J., Reed, K. A., Bao, Q., Barsugli, J. J., Camargo, S. J., Caron, L.-P., Chang, P., Chen, C.-T.,  
1006 Christensen, H. M., Danabasoglu, G., Frenger, I., Fučkar, N. S., ul Hasson, S., Hewitt, H. T., Huang,  
1007 H., Kim, D., Kodama, C., Lai, M., Leung, L.-Y. R., Mizuta, R., Nobre, P., Ortega, P., Paquin, D.,  
1008 Roberts, C. D., Scoccimarro, E., Seddon, J., Treguier, A. M., Tu, C.-Y., Ullrich, P. A., Vidale, P. L.,  
1009 Wehner, M. F., Zarzycki, C. M., Zhang, B., Zhang, W., and Zhao, M.: High-Resolution model

1010 intercomparison project phase 2 (HighResMIP2) towards CMIP7, *Geoscientific Model*  
1011 *Development*, 18, 1307–1332, <https://doi.org/10.5194/gmd-18-1307-2025>, 2025.

1012 Rong, X. Y., Zhang, R. H., Li, T., and Su, J. Z.: Upscale feedback of high-frequency winds to ENSO,  
1013 *Quarterly Journal of the Royal Meteorological Society*, 137, 894–907,  
1014 <https://doi.org/10.1002/qj.804>, 2011.

1015 Savarin, A. and Chen, S. S.: Pathways to better prediction of the MJO: I. Effects of model resolution and  
1016 moist physics on Atmospheric boundary layer and precipitation, *Journal of Advances in Modeling*  
1017 *Earth Systems*, 14, e2021MS002928, <https://doi.org/10.1029/2021ms002929>, 2022.

1018 Small, R. J., Bryan, F. O., Bishop, S. P., and Tomas, R. A.: Air–Sea turbulent heat fluxes in climate models  
1019 and observational analyses: What drives their variability?, *Journal of Climate*, 32, 2397–2421,  
1020 <https://doi.org/10.1175/jcli-d-18-0576.1>, 2019.

1021 Song, M.: The code of FGOALS-f3 model study, Zenodo [code],  
1022 <https://doi.org/10.5281/zenodo.17778266>, 2025.

1023 Su, J. Z., Zhang, R. H., Li, T., Rong, X. Y., Kug, J. S., and Hong, C.-C.: Causes of the El Niño and La  
1024 Niña amplitude asymmetry in the equatorial eastern Pacific, *Journal of Climate*, 23, 605–617,  
1025 <https://doi.org/10.1175/2009jcli2894.1>, 2010.

1026 Su, J. Z., Li, T., and Zhang, R. H.: The initiation and developing mechanisms of central Pacific El Niños,  
1027 *Journal of Climate*, 27, 4473–4485, <https://doi.org/10.1175/jcli-d-13-00640.1>, 2014.

1028 Sun, M., Li, T., and Chen, L.: El Niño phase-dependent high-frequency variability in western equatorial  
1029 Pacific, *Climate Dynamics*, 55, 2165–2184, <https://doi.org/10.1007/s00382-020-05376-2>, 2020.

1030 Tang, Y. L., HuangFu, J. I., Huang, R. H., and Chen, W.: Simulation and projection of tropical cyclone  
1031 activities over the western North Pacific by CMIP6 HighResMIP, *Climate Dynamics*, 35, 7771–  
1032 7794, <https://doi.org/10.1175/JCLI-D-21-0760.1>, 2022.

1033 Thomson, D. J.: Spectrum estimation and harmonic analysis, *Proceedings of the IEEE*, 79, 1055-1096,  
1034 <https://doi.org/10.1109/PROC.1982.12433>, 1982.

1035 Timmermann, A., An, S. I., Kug, J. S., Jin, F. F., Cai, W., Capotondi, A., Cobb, K. M., Lengaigne, M.,  
1036 McPhaden, M. J., Stuecker, M. F., Stein, K., Wittenberg, A. T., Yun, K. S., Bayr, T., Chen, H. C.,  
1037 Chikamoto, Y., Dewitte, B., Dommenges, D., Grothe, P., Guilyardi, E., Ham, Y. G., Hayashi, M.,  
1038 Ineson, S., Kang, D., Kim, S., Kim, W., Lee, J. Y., Li, T., Luo, J. J., McGregor, S., Planton, Y., Power,

1039 S., Rashid, H., Ren, H. L., Santoso, A., Takahashi, K., Todd, A., Wang, G., Wang, G., Xie, R., Yang,  
1040 W. H., Yeh, S. W., Yoon, J., Zeller, E., and Zhang, X.: El Nino-Southern Oscillation complexity,  
1041 Nature, 559, 535–545, <https://doi.org/10.1038/s41586-018-0252-6>, 2018.

1042 Wang, L., Li, T., and Zhou, T. J.: Intraseasonal SST variability and air-sea interaction over the Kuroshio  
1043 extension region during boreal summer. Journal of Climate, 25, 1619–1634,  
1044 <https://doi.org/10.1175/JCLI-D-11-00109.1>, 2012.

1045 Wei, X. J. Chen, L., and Sun, M.: Fine-tuning Atmospheric Parameters for Improving ENSO Simulation  
1046 in the Zebiak–Cane Model, Advances in Atmospheric Science, 43, 420–435,  
1047 <https://doi.org/10.1007/s00376-025-4423-8>, 2026.

1048 Yan, Y. and Sun, D.-Z.: Phase-Locking of El Niño and La Niña events in CMIP6 models, Atmosphere,  
1049 15, 882, <https://doi.org/10.3390/atmos15080882>, 2024.

1050 Ying, J., Lian, T., Ren, H.-L., Zhang, C., Liu, T., and Tan, X.-X.: Effects of tropical cyclones on ENSO,  
1051 Journal of Climate, 32, 6423–6443, <https://doi.org/10.1175/jcli-d-18-0821.1>, 2019.

1052 Ying, M., Zhang, W., Yu, H., Lu, X. Q., Feng, J. X., Fan, Y. X., Zhu, Y. t., and Chen, D. Q.: An overview  
1053 of the China Meteorological Administration tropical cyclone database, Journal of Atmospheric and  
1054 Oceanic Technology, 31, 287–301, <https://doi.org/https://10.1175/JTECH-D-12-00119.1>, 2014.

1055 Yu, Y. Q., An, B., Liu, H. L., Bao, Q., Lin, P. F., He, B., Zheng, W. P., Luan, Y. H., Bai, R. and Li, T. Y.:  
1056 Review of the development and application of the high-resolution climate system model FGOALS,  
1057 Chinese Journal of Atmospheric Sciences (in Chinese), 48, 200-217,  
1058 <https://doi.org/10.1007/BF02915571>, 2024.

1059 Yu, Y. Q., Tang, S. L., Liu, H. L., Lin, P. F., and Li, X. L.: Development and evaluation of the dynamic  
1060 framework of an ocean general circulation model with arbitrary orthogonal curvilinear coordinate,  
1061 Chinese Journal of Atmospheric Sciences (in Chinese), 42, 877–889,  
1062 <https://doi.org/10.3878/j.issn.1006-9895.1805.17284>, 2018.

1063 Zhang, R.-H., Yu, Y. Q., Song, Z. Y., Ren, H.-L., Tang, Y. M., Qiao, F. l., Wu, T. W., Gao, C., Hu, J. Y.,  
1064 Tian, F., Zhu, Y. C., Chen, L., Liu, H. L., Lin, P. F., Wu, F. H., and Wang, L.: A review of progress  
1065 in coupled ocean-atmosphere model developments for ENSO studies in China, Journal of  
1066 Oceanology and Limnology, 38, 930–961, <https://doi.org/10.1007/s00343-020-0157-8>, 2020.

1067 Zhao, J. W., Wang, F., Zhan, R. F., Guo, Y. P., Huang, X., and Liu, C.: How Does Tropical Cyclone

1068 Genesis Frequency Respond to a Changing Climate?, *Geophysical Research Letters*, 50,  
1069 <https://doi.org/10.1029/2023gl102879>, 2023.

1070 Zhao, Y. D. and Sun, D.-Z.: ENSO asymmetry in CMIP6 models, *Journal of Climate*, 35, 5555–5572,  
1071 <https://doi.org/10.1175/jcli-d-21-0835.1>, 2022.

1072 Zhou, L., Bao, Q., Liu, Y. M., Wu, G. X., Wang, W. C., Wang, X. C., He, B., Yu, H. Y., and Li, J. D.:  
1073 Global energy and water balance: Characteristics from Finite-volume Atmospheric Model of the  
1074 IAP/LASG (FAMIL 1), *Journal of Advances in Modeling Earth Systems*, 7, 1–20,  
1075 <https://doi.org/10.1002/2014MS000349>, 2015.

1076 Zi, P., Liu, Y. M., Li, J. D., Yang, R. W., He, B., and Bao, Q.: Reduced Spring Precipitation Bias and  
1077 Associated Physical Causes over South China in FGOALS-f3 Climate Models: Experiments with  
1078 the Horizontal Resolutions, *Journal of Meteorological Research*, 38, 784–804,  
1079 <https://doi.org/10.1007/s13351-024-3200-4>, 2024.

1080 Zuo, H., Balmaseda, M. A., Tietsche, S., Mogensen, K., and Mayer, M.: The ECMWF operational  
1081 ensemble reanalysis–analysis system for ocean and sea ice: A description of the system and  
1082 assessment, *Ocean Science*, 15, 779–808, <https://doi.org/10.5194/os-15-779-2019>, 2019.